Article

Current Biology

Increased LRRK2 kinase activity alters neuronal autophagy by disrupting the axonal transport of autophagosomes

Graphical abstract

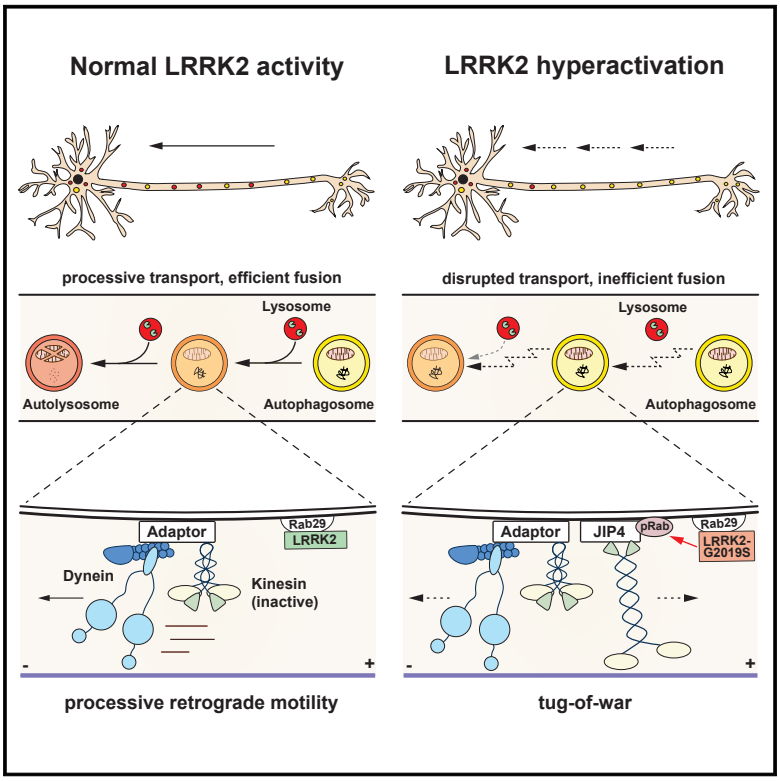

Authors

C. Alexander Boecker, Juliet Goldsmith, Dan Dou, Gregory G. Cajka, Erika L.F. Holzbaur

Correspondence

holzbaur@pennmedicine.upenn.edu

In brief

Boecker et al. find that hyperactivation of LRRK2 by a Parkinson's disease-associated mutation disrupts the axonal transport of autophagosomes through the dysregulation of associated motors. Defective transport leads to impaired autophagosome maturation. Thus, dysfunctional autophagy is predicted to contribute to Parkinson's disease pathogenesis.

Highlights

- Parkinson's disease LRRK2-G2019S mutation disrupts axonal autophagosome transport
- Rab29-induced LRRK2 hyperactivation also impairs autophagosome transport
- Hyperactive LRRK2 recruits JIP4, causing a tug of war between autophagosome motors
- Impaired axonal transport is accompanied by defective autophagosome acidification

Boecker et al., 2021, Current Biology *31*, 2140–2154
May 24, 2021
https://doi.org/10.1016/j.cub.2021.02.061

CellPress

CellPress
OPEN ACCESS

Current Biology

Article

Increased LRRK2 kinase activity alters neuronal autophagy by disrupting the axonal transport of autophagosomes

C. Alexander Boecker,[1] Juliet Goldsmith,[1] Dan Dou,[1] Gregory G. Cajka,[2] and Erika L.F. Holzbaur[1,3,*]
[1]Department of Physiology, Perelman School of Medicine, University of Pennsylvania, Philadelphia, PA 19104, USA
[2]Department of Genetics, Perelman School of Medicine, University of Pennsylvania, Philadelphia, PA 19104, USA
[3]Lead contact
*Correspondence: holzbaur@pennmedicine.upenn.edu
https://doi.org/10.1016/j.cub.2021.02.061

SUMMARY

Parkinson's disease-causing mutations in the leucine-rich repeat kinase 2 (*LRRK2*) gene hyperactivate LRRK2 kinase activity and cause increased phosphorylation of Rab GTPases, important regulators of intracellular trafficking. We found that the most common LRRK2 mutation, LRRK2-G2019S, dramatically reduces the processivity of autophagosome transport in neurons in a kinase-dependent manner. This effect was consistent across an overexpression model, neurons from a G2019S knockin mouse, and human induced pluripotent stem cell (iPSC)-derived neurons gene edited to express the G2019S mutation, and the effect was reversed by genetic or pharmacological inhibition of LRRK2. Furthermore, LRRK2 hyperactivation induced by overexpression of Rab29, a known activator of LRRK2 kinase, disrupted autophagosome transport to a similar extent. Mechanistically, we found that hyperactive LRRK2 recruits the motor adaptor JNK-interacting protein 4 (JIP4) to the autophagosomal membrane, inducing abnormal activation of kinesin that we propose leads to an unproductive tug of war between anterograde and retrograde motors. Disruption of autophagosome transport correlated with a significant defect in autophagosome acidification, suggesting that the observed transport deficit impairs effective degradation of autophagosomal cargo in neurons. Our results robustly link increased LRRK2 kinase activity to defects in autophagosome transport and maturation, further implicating defective autophagy in the pathogenesis of Parkinson's disease.

INTRODUCTION

The leucine-rich repeat kinase 2 (*LRRK2*) gene encodes a large multidomain protein linked to the pathogenesis of Parkinson's disease (PD).[1] LRRK2 mutations are the most common genetic cause of PD, accounting for ~1% of sporadic and ~5% of familial forms.[2] The most frequent pathogenic mutation, LRRK2-G2019S, is an autosomal dominant missense mutation located in the kinase domain that enhances kinase activity.[3–5] Increased LRRK2 kinase activity is also induced by a PD-causing mutation in the *VPS35* gene[6] and has been observed in patients with idiopathic PD.[7] Together, these observations indicate that elevated activation of LRRK2 kinase may be a common pathogenic driver of PD, although the mechanism by which increased LRRK2 activity leads to neurodegeneration remains unknown.

Phospho-proteomic analyses identified a subset of Rab GTPases, including Rab8, Rab10, and Rab29, as bona fide substrates of LRRK2 kinase.[8,9] Rab proteins are master regulators of intracellular trafficking.[10] Increased LRRK2 kinase activity enhances Rab phosphorylation, altering interactions with downstream effector proteins such as the motor adaptor protein JNK-interacting protein 4 (JIP4).[11,12] In particular, Rab29 is genetically linked to PD[13] and functions as both a substrate and activator of LRRK2 kinase.[14–16]

Effective intracellular transport is essential for neurons because of their unique morphology with an axonal arbor estimated to range up to hundreds of meters in total length within the human CNS.[17] The extensive axonal arborization of dopaminergic nigrostriatal neurons may make these cells especially vulnerable to transport deficits.[18,19] In particular, axonal transport of autophagic vesicles (AVs) in neurons is tightly regulated and vital to neuronal homeostasis.[20,21] AVs are preferentially formed at the distal tip of the axon and then transported retrogradely toward the cell soma, maturing *en route* by fusion with late endosomes/lysosomes.[21–24] Inhibition of AV transport impairs AV acidification, causing defective cargo degradation.[24,25] Defects in autophagy have repeatedly been linked to PD in general and to LRRK2-mediated pathophysiology in particular.[26–30]

Here, we investigated the effects of the LRRK2-G2019S mutation on organelle transport and neuronal autophagy. We examined three model systems: LRRK2-G2019S overexpression, primary G2019S knockin (KI) neurons,[31,32] and gene-edited human induced pluripotent stem cell (iPSC)-derived G2019S KI neurons. In all three models, LRRK2-G2019S decreased the processivity of AV transport through increased kinase activity. Impaired AV transport was accompanied by defects in axonal AV acidification, indicating defective AV maturation. LRRK2 hyperactivation induced by Rab29 overexpression decreased the

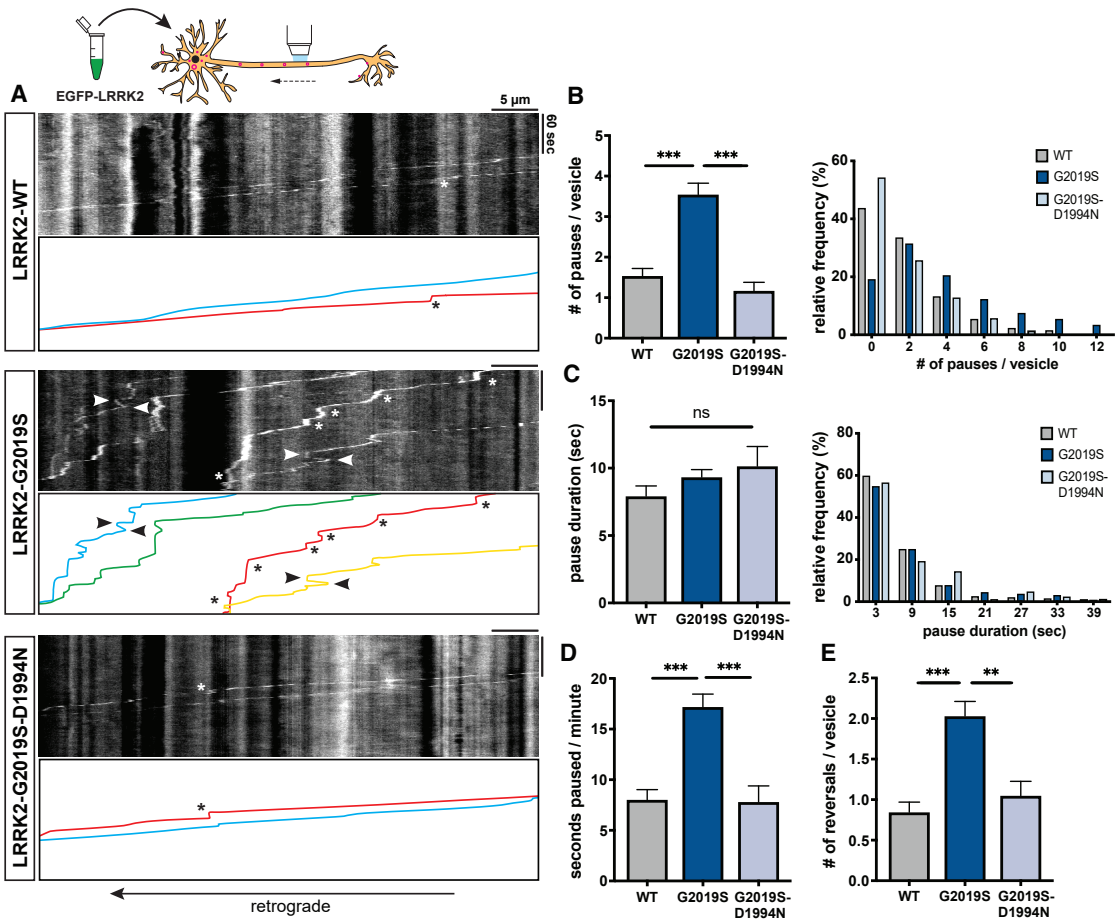

Figure 1. Overexpression of LRRK2-G2019S disrupts processivity of axonal AV transport

(A) Kymographs of mCherry-LC3 vesicles in EGFP-LRRK2-WT-, EGFP-LRRK2-G2019S-, and EGFP-LRRK2-G2019S-D1994N-expressing axons. Asterisks indicate pauses. Arrowheads point to reversals. See also Video S1.

(B and C) Bar graph and frequency distribution of (B) pause number per vesicle and (C) pause duration during AV transport in WT, G2019S-, and G2019S-D1994N-expressing neurons. Frequency distribution does not show pauses >42 s (WT: 2.54%; G2019S: 2.87%; G2019S-D1994N: 3.49%).

(D) Fraction of time paused (as measured by seconds paused per minute).

(E) Number of reversals per AV in WT, G2019S-, and G2019S-D1994N-expressing axons (mean ± SEM; n = 87–139 AVs from 17–20 neurons from 3 independent cultures; ns, not significant, p = 0.44; **p = 0.0008; ***p < 0.0001; Kruskal-Wallis with Dunn's multiple comparisons test).

See also Figures S1A–S1C for quantification of AV directionality and density. Figures S3A–S3H and S4I–S4M show the effect of LRRK2-G2019S overexpression on microtubule and LAMP1-vesicle dynamics, respectively.

processivity of AV transport to a similar extent. Downstream of hyperactive LRRK2, our data implicate the enhanced recruitment of the kinesin-activating motor adaptor protein JIP4 in the disruption of AV transport, resulting in an unregulated tug of war between anterograde and retrograde motors. Our data linking LRRK2 hyperactivation to the defective trafficking of neuronal autophagosomes further establish autophagy as a key pathway in PD pathogenesis.

RESULTS

Overexpression of LRRK2-G2019S disrupts the processivity of AV transport

Given the data implicating LRRK2 in the regulation of autophagy, we asked whether overexpression of LRRK2-G2019S affects axonal AV transport.[26–30] Rat hippocampal neurons were transfected with EGFP-LRRK2-WT (wild type) or EGFP-LRRK2-G2019S. In parallel, we used the kinase-inactive variant EGFP-LRRK2-G2019S-D1994N to assess the dependency of the effect of LRRK2-G2019S on its increased kinase activity (Figure 1A). In all three groups, most mCherry-LC3-labeled AVs were transported retrogradely (~80%; Figures S1A and S1B), as previously described in neurons both *in vitro* and *in vivo*.[21–24,33,34] The density of AVs in the mid-axon was similar in all groups (Figure S1C), suggesting that neither overexpression of hyperactive nor kinase-dead LRRK2 affects the overall rate of autophagosome production in the distal axon.

Strikingly, we observed that AVs in neurons expressing LRRK2-G2019S paused frequently during retrograde organelle motility (Figure 1A; Video S1). The number of pauses per vesicle in LRRK2-G2019S-expressing neurons was more than 2-fold higher than in neurons expressing LRRK2-WT (Figure 1B). By

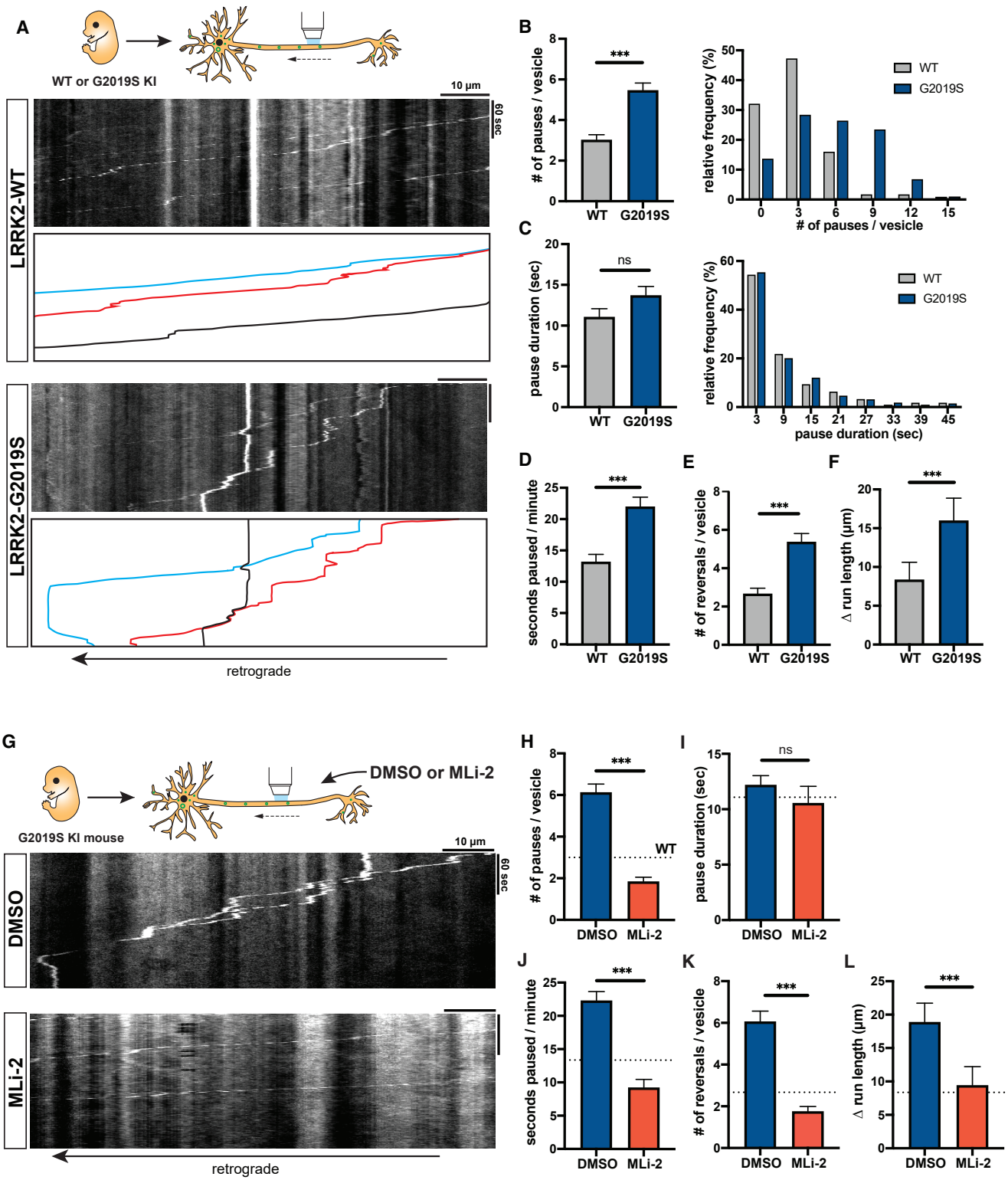

Figure 2. AV transport is disrupted in mouse LRRK2-G2019S KI neurons and rescued by LRRK2 kinase inhibition

(A) Kymographs of axonal EGFP-LC3 vesicles in WT and G2019S knockin (KI) mouse cortical neurons. See also Video S2.

(B and C) Bar graph and frequency distribution of (B) pause number per vesicle and (C) pause duration during AV transport in WT and G2019S KI neurons. Frequency distribution does not show pauses >48 s (WT: 2.95%; G2019S: 6.89%).

(legend continued on next page)

contrast, AVs in LRRK2-G2019S-D1994N neurons paused at a similar frequency as in LRRK2-WT neurons (Figure 1B), suggesting that increased pausing is dependent on the hyperactive kinase activity of LRRK2-G2019S. The average pause duration in LRRK2-G2019S neurons was not significantly different from LRRK2-WT or LRRK2-G2019S-D1994N cells (Figure 1C), but because of the higher frequency of pauses, the fraction of time paused per vesicle was significantly increased (Figure 1D). AVs in LRRK2-G2019S neurons also changed direction more frequently (Figure 1A; Video S1). The number of reversals was significantly increased in LRRK2-G2019S neurons compared with either LRRK2-WT or LRRK2-G2019S-D1994N (Figure 1E).

Endogenous LRRK2-G2019S disrupts AV transport in mouse cortical neurons and iPSC-derived neurons in a kinase-dependent manner

Next, we investigated whether LRRK2-G2019S affects axonal AV transport when expressed at endogenous levels. Western blots confirmed similar LRRK2 expression levels in cortical neurons from WT or G2019S KI mice (Figures S1D and S1E). In both WT and G2019S KI neurons, the majority of axonal EGFP-LC3-labeled AVs moved in the retrograde direction (Figure S1F). The number of pauses during AV transport was significantly increased in G2019S KI neurons, with AVs pausing ~2 times more frequently (Figures 2A and 2B; Video S2). The average pause duration was not affected (Figure 2C). Thus, the increased fraction of time paused of AVs in G2019S KI neurons (Figure 2D) is due to the higher pause number. The number of reversals during AV transport was also significantly increased in G2019S KI neurons (Figure 2E). To quantify how this higher number of reversals affects the overall processivity of AV transport, we calculated the difference between total and net run length of each vesicle (Δ run length; Figure S1G). To ensure robust run length quantification, we imaged for longer time periods and with a larger field of view. Notably, Δ run length was significantly higher in G2019S KI neurons, indicating a loss of directed processivity in AV transport due to an increase of non-processive motility (Figure 2F).

To investigate whether the loss of processivity was caused by increased LRRK2 activity, we tested whether the LRRK2 kinase inhibitor MLi-2[35] rescues AV transport in G2019S KI neurons. Treatment with 100 nM MLi-2 markedly decreased LRRK2 kinase activity in G2019S KI neurons, as measured by reduced levels of LRRK2-phosphorylated phosphothreonine-73 (pT73) Rab10 and phosphoserine-106 (pS106) Rab12 (Figures S2A and S2B). LRRK2 inhibition by MLi-2 significantly reduced pause number and fraction of time paused for axonal AVs in G2019S KI neurons (Figures 2G–2J; Video S3). Both parameters were reduced to levels lower than in untreated WT neurons (see dotted lines in Figures 2H–2L). MLi-2 treatment also rescued non-processive motility in G2019S KI neurons, as measured by number of reversals and Δ run length (Figures 2K and 2L).

As a third independent model, we investigated the effect of G2019S mutation on AV transport in human iPSC-derived neurons (i^{3}Neurons),[34,36] which have been shown to express LRRK2.[37] We used CRISPR/Cas9 gene editing to generate i^{3}N iPSCs heterozygous for the G2019S mutation. EGFP-LC3 labeled AVs in G2019S KI i^{3}Neurons paused significantly more frequently than in isogenic WT i^{3}Neurons (Figures 3A and 3B; Video S4). While the average pause duration was not affected by the G2019S mutation (Figure 3C), the fraction of time paused, number of reversals, and Δ run length were significantly increased (Figures 3D–3F). Treatment with 100 nM MLi-2 rescued the number of pauses and fraction of time paused in G2019S KI i^{3}Neurons (Figures 3G–3J). While MLi-2 did not have a significant effect on Δ run length, it reduced the number of reversals to a similar level as observed in WT neurons (Figures 3K and 3L). Thus, consistent with the data from overexpression model and mouse G2019S KI neurons, we observed a significant disruption of AV transport in human G2019S KI neurons that was rescued by pharmacological LRRK2 kinase inhibition.

LRRK2-G2019S does not affect axonal microtubule dynamics

Previous reports have proposed that LRRK2 mutants may alter microtubule dynamics by affecting microtubule stability, which could potentially contribute to the defects in AV transport we observed.[38–40] We expressed fluorescently labeled end-binding protein 3 (EB3) in mouse WT and G2019S KI neurons to visualize the plus ends of growing microtubules and measure microtubule dynamics (Figure S2C). Quantification revealed no differences in run length, run time, velocity, or density of EB3 comets between WT and G2019S KI neurons (Figures S2D–S2G). Similarly, overexpression of EGFP-LRRK2-WT or EGFP-LRRK2-G2019S in rat hippocampal neurons did not affect run length, run time, or number of EB3 comets compared with the expression of EGFP only (Figures S3A–S3H).

Since the LRRK2 inhibitor MLi-2 has been shown to increase the affinity of LRRK2 for microtubules,[41] we investigated whether MLi-2 treatment affects microtubule dynamics at endogenous LRRK2 expression levels. We observed no differences in run time, run length, velocity, or density of EB3 comets between DMSO- or MLi-2-treated mouse WT neurons (Figures S3I–S3P).

LRRK2-G2019S does not affect axonal transport of LAMP1 vesicles

To investigate whether LRRK2-G2019S affects the axonal transport of other cargoes, we examined the motility of lysosomal-associated membrane protein 1 (LAMP1)-RFP-positive

(D–F) Fraction of time paused (D), number of reversals (E), and Δ run length (difference between total run length and net run length) (F) of AVs in WT and G2019S KI neurons (mean ± SEM; n = 112–126 AVs from 26 neurons from 3 independent cultures; ns, not significant, p = 0.78; ***p < 0.0001; Mann-Whitney test). Figures S1D–S1G show LRRK2 expression and AV directionality in WT and G2019S KI neurons.

(G) Kymographs of axonal EGFP-LC3 vesicles in mouse G2019S KI neurons treated overnight with DMSO or 100 nM MLi-2. See also Video S3.

(H–L) Pause number (H), pause duration (I), fraction of time paused (J), number of reversals (K), and Δ run length (L) of AVs in G2019S KI neurons treated with DMSO or MLi-2 (mean ± SEM; n = 106-116 AVs from 24 to 28 neurons from 3 independent cultures; ns, not significant, p = 0.02; ***p < 0.0001; Mann-Whitney test with Bonferroni correction for multiple testing: p < 0.0125 was considered statistically significant). Dotted lines indicate the respective average observed in untreated WT neurons. See also Figures S2A and S2B for phospho-Rab western blots of WT or G2019S KI neurons ± MLi-2.

Microtubule dynamics in G2019S KI neurons and the effect of MLi-2 on microtubule dynamics are shown in Figures S2C–S2G and S3I–S3P. Figure S4A–S4G show LAMP1-vesicle dynamics in G2019S KI neurons.

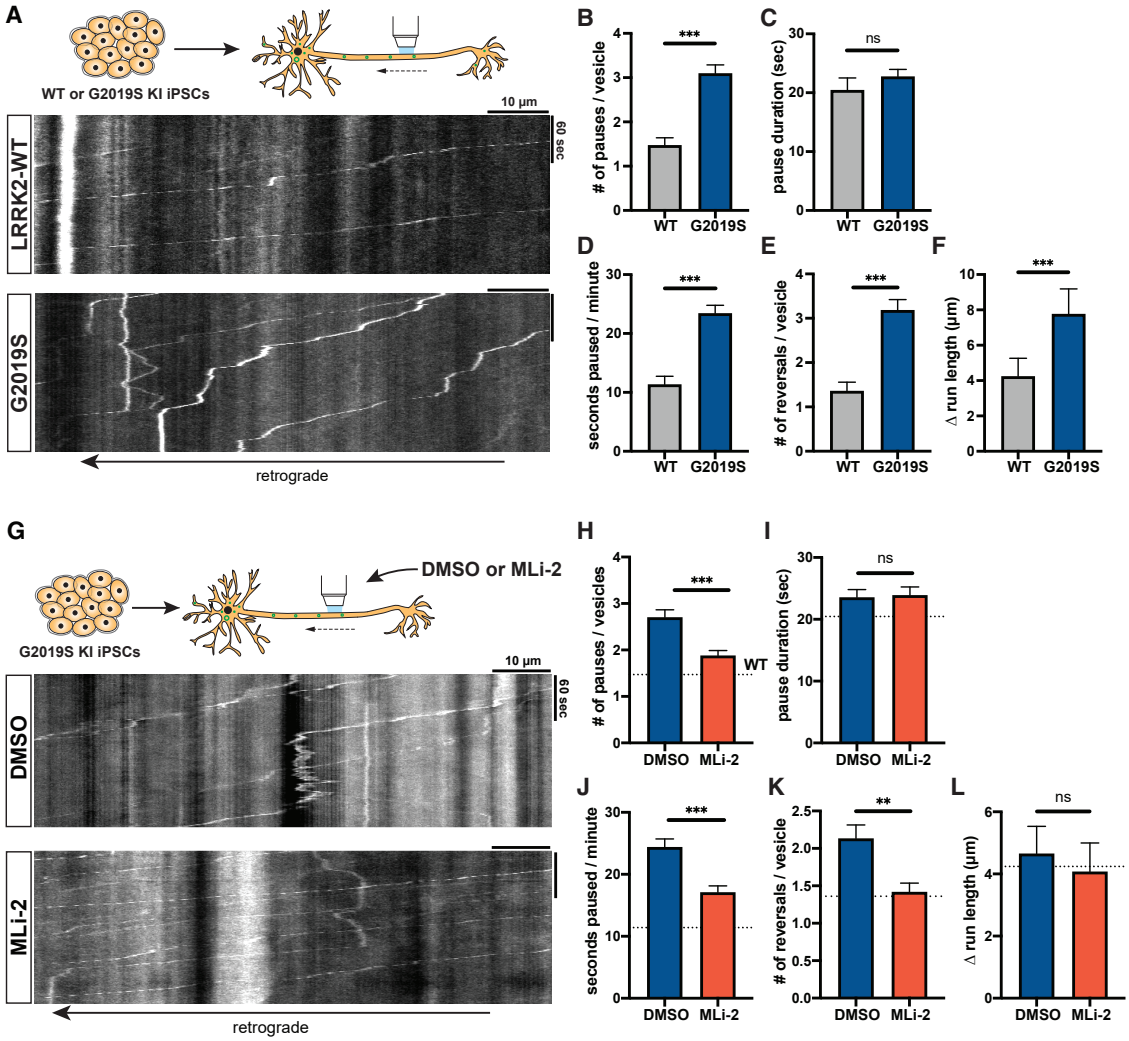

Figure 3. AV transport is disrupted in human iPSC-derived LRRK2-G2019S KI neurons and rescued by LRRK2 kinase inhibition

(A) Kymographs of axonal EGFP-LC3 vesicles in WT and G2019S KI i^{3}Neurons. See also Video S4.

(B–F) Pause number (B), pause duration (C), fraction of time paused (D), number of reversals (E), and Δ run length (F) of AVs in WT and G2019S KI i^{3}Neurons (mean ± SEM; n = 133–189 AVs from 32 to 33 neurons from 3 independent experiments; ns, not significant, p = 0.0299; ***p < 0.0001; Mann-Whitney test with Bonferroni correction for multiple testing: p < 0.0125 was considered statistically significant).

(G) Kymographs of axonal EGFP-LC3 vesicles in G2019S KI i^{3}Neurons treated overnight with DMSO or 100 nM MLi-2.

(H–L) Pause number (H), pause duration (I), fraction of time paused (J), number of reversals (K), and Δ run length (L) of AVs in G2019S KI i^{3}Neurons treated with DMSO or MLi-2 (mean ± SEM; n = 225–279 AVs from 41 to 43 neurons from 3 independent cultures; ns, not significant, p > 0.1368; **p = 0.0021; ***p = 0.0001; Mann-Whitney test). Dotted lines indicate the respective average in untreated WT i^{3}Neurons.

late endosomes/lysosomes in WT and G2019S KI neurons. First, we photobleached a segment of the axon to deplete the signal of stationary vesicles,[42] aiding visualization of mobile vesicles and allowing quantification of pause events (Figure S4A). In contrast to the robust retrograde motility of AVs, about two-thirds of mobile LAMP1 vesicles moved in the anterograde direction (Figure S4G). Measurements of pausing for motile LAMP1 vesicles revealed no difference between WT and G2019S KI neurons (Figures S4B and S4C). Analysis of retrograde LAMP1 vesicles only showed a small but nonsignificant trend toward a higher pause number and higher fraction of time paused in G2019S KI neurons (Figures S4D and S4E). Co-expression of EGFP-LC3 and LAMP1-RFP showed that only a small fraction of retrograde LAMP1-RFP vesicles was positive for EGFP-LC3 (~13%; Figure S4H). Similar to the observations in G2019S KI neurons, overexpression of LRRK2-G2019S did not significantly alter axonal trafficking of LAMP1-RFP vesicles in rat hippocampal neurons (Figures S4I–S4M).

Impairment of axonal transport by LRRK2-G2019S affects maturation of axonal AVs

Retrograde transport facilitates AV maturation in the axon through *en route* fusion with lysosomal vesicles. Disrupted AV transport has been shown to impair AV acidification, leading to defective cargo degradation.[25,43] To probe whether LRRK2-G2019S affects AV maturation, we transfected mouse WT or G2019S KI neurons

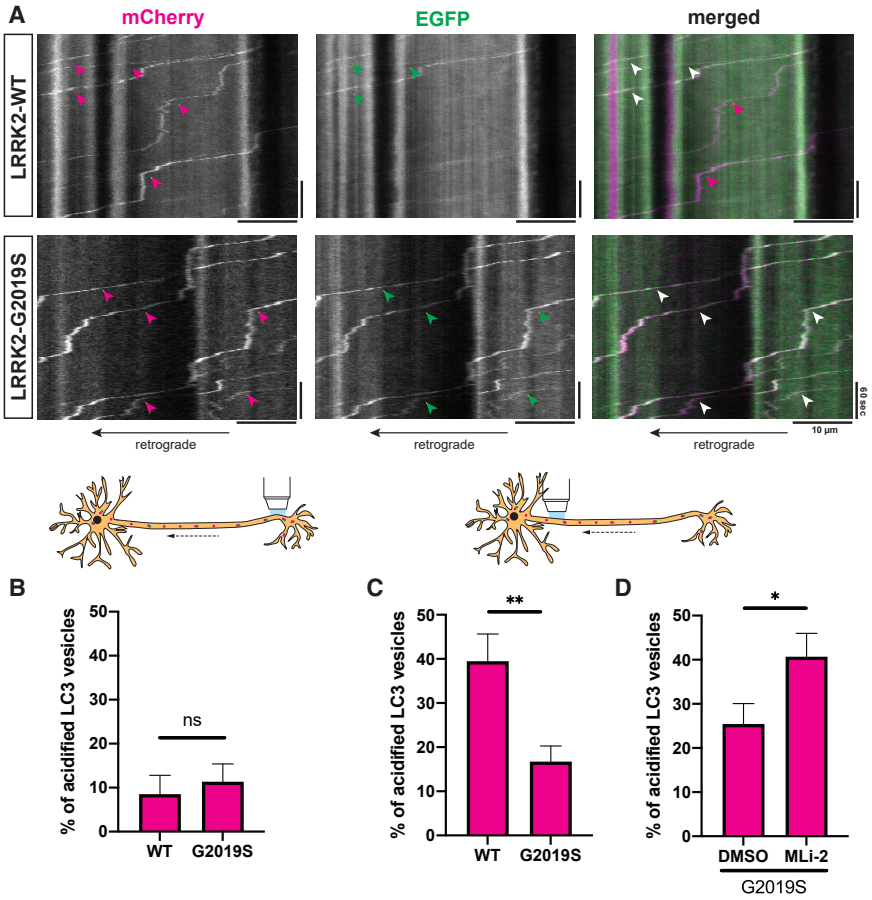

Figure 4. LRRK2-G2019S disrupts acidification of axonal AVs

(A) Kymographs of mCherry-EGFP-LC3 vesicles in the proximal axon of WT or G2019S KI mouse cortical neurons. Magenta arrowheads, mCherry-positive traces; green arrowheads, EGFP-positive traces; white arrowheads, mCherry- and EGFP-positive traces.

(B–D) Percentage of acidified (=mCherry-only-positive) AVs in (B) the distal (mean ± SEM; n = 17–20 neurons from 4 independent cultures; ns, not significant, p = 0.55; Mann-Whitney test); (C) the proximal axon of WT and G2019S KI neurons (mean ± SEM; n = 29–30 neurons from 4 independent cultures; **p = 0.0084; Mann-Whitney test); and (D) the proximal axon of G2019S KI neurons treated with DMSO or 100 nM MLi-2 overnight (mean ± SEM; n = 24–26 neurons from 3 independent cultures; *p = 0.0123; Mann-Whitney test).

For acidification of axonal LAMP1 vesicles, see Figures S5C–S5E.

with mCherry-EGFP-LC3 (Figure 4A). The EGFP signal of this tandem construct is quenched in an acidic environment, allowing for differentiation between non-acidified (mCherry- and EGFP-positive) and acidified (mCherry-only-positive) LC3 vesicles.

In the distal axon of both WT and G2019S KI neurons, only ~10% of AVs were acidified (Figure 4B). This is not surprising, as *de novo* formation of immature AVs takes place at the distal tip.[22,44] Consistent with AV maturation during retrograde transport, we observed a higher fraction of acidified AVs in the proximal axon. However, the fraction of acidified AVs in the proximal axon of G2019S KI neurons (~20%) was significantly lower than in WT neurons (~40%) (Figures 4A and 4C). LRRK2 inhibition by MLi-2 fully rescued impaired AV acidification in the proximal axon of G2019S KI neurons (Figure 4D). Impairment of autophagosome transport and acidification correlated with a trend toward a higher number of LC3 vesicles in the proximal axon of G2019S KI neurons (Figure S5A). Treatment with MLi-2 significantly decreased the number of LC3 vesicles in the proximal axon of G2019S KI neurons (Figure S5B). Together, these findings demonstrate that G2019S mutation substantially impairs the maturation of axonal AVs in a kinase-dependent manner.

In contrast to AV transport, axonal trafficking of LAMP1-positive late endosomes/lysosomes was not affected by expression of the G2019S mutation (Figure S4). Furthermore, using superecliptic pHluorin (SEP)-LAMP1-RFP as a dual-color reporter for late endosome/lysosome acidification,[45,46] we did not observe a difference in the acidification of axonal LAMP1 vesicles between WT and G2019S KI neurons (Figures S5C–S5E). These findings suggest that impaired AV acidification in G2019S KI neurons was not induced by lysosomal defects.

Rab29 is localized to axonal AVs

Rab29 functions as both a substrate and an activator of LRRK2 kinase.[8,14,16,32,47] Overexpression of Rab29 has been shown to increase LRRK2 kinase activity.[14,16] To investigate whether Rab29 may be involved in the LRRK2 pathway controlling processivity of AV transport, we transiently expressed EGFP-Rab29 together with mCherry-LC3 in mouse cortical neurons. Intriguingly, we observed robust comigration of EGFP-Rab29 with axonal LC3 vesicles (Figure 5A; Video S5). We also noticed a distinct population of dimmer EGFP-Rab29 vesicles moving along the axon that did not colocalize with LC3-positive AVs (Figures 5A and 5G). Consistent with previous observations in cell lines,[14,16] there was a Golgi-like distribution of EGFP-Rab29 in the neuronal soma (Figure S6A), spatially separated from the axonal, AV-associated population.

The observed colocalization of Rab29 and LC3 in the axon could be explained by either an association of Rab29 with the outer AV membrane or by engulfment of Rab29 within the AV lumen as an autophagosomal cargo. To distinguish between these possibilities, we photobleached Halo-Rab29 on EGFP-LC3-positive axonal AVs and analyzed fluorescence recovery. We observed that Halo-Rab29 signal recovered over several minutes (Figures 5B and S6B; Video S6). This indicates that photobleached Halo-Rab29 is gradually replaced by fluorescent Halo-Rab29 from the cytosol, suggesting that Rab29 is bound to the outer AV membrane. If Rab29 was located in the AV lumen, fluorescence recovery would not be observed. Quantification of Halo-Rab29 intensity after photobleaching showed a similar recovery in WT and G2019S KI neurons (Figure S6C).

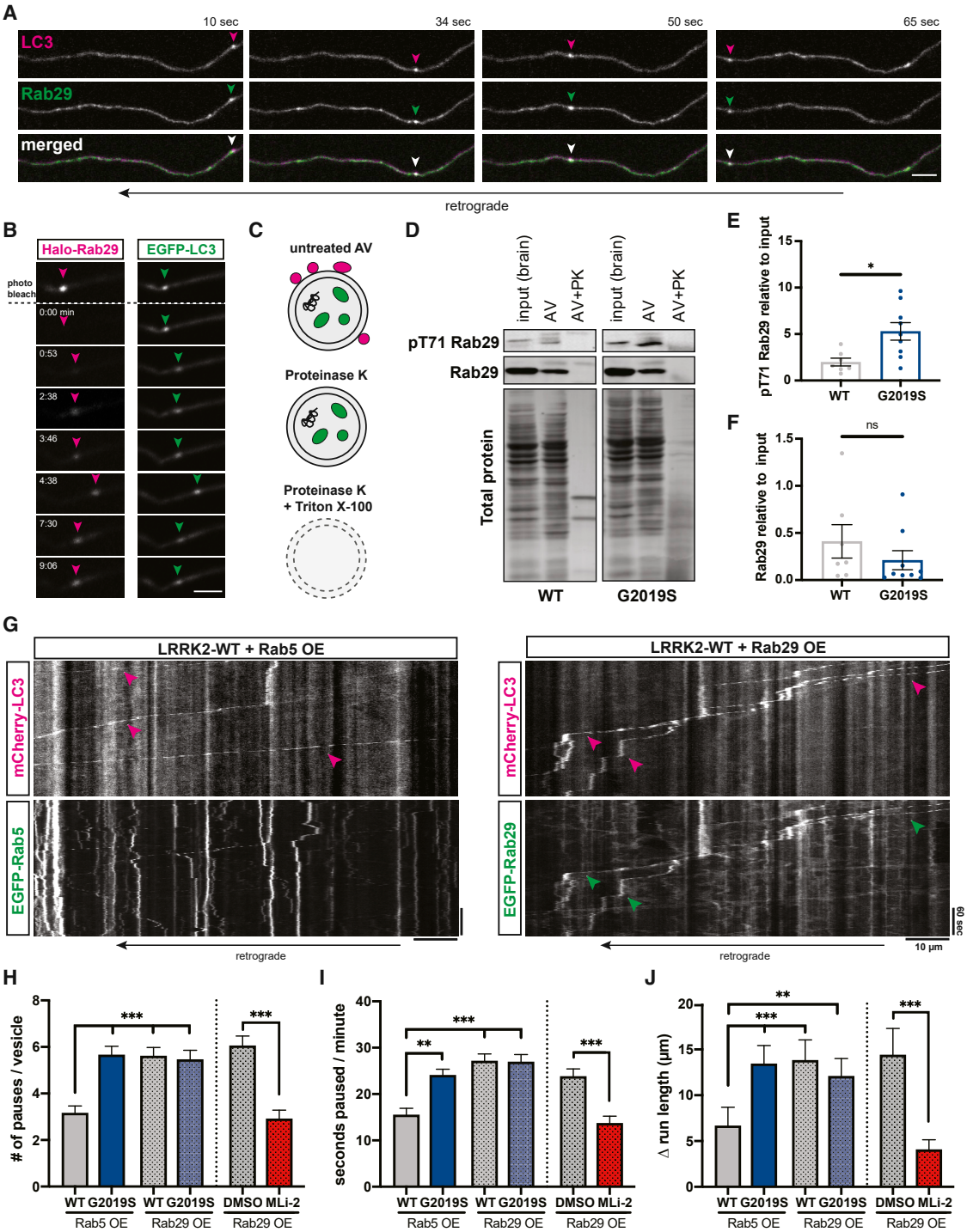

Figure 5. Overexpression of Rab29 disrupts AV transport

(A) Time-lapse images of axonal mCherry-LC3 and EGFP-Rab29 vesicles in a WT mouse cortical neuron. Scale bar, 5 µm. See also Video S5.

(B) Fluorescence recovery after photobleaching Halo-Rab29 signal of an EGFP-LC3-labeled AV. Arrowheads point to the position of the AV. Scale bar, 5 µm. See also Figures S6A–S6C and Video S6.

(C) Proteins associated with the outer membrane of isolated AVs are degraded after treatment with Proteinase K (PK). AV cargo is only degraded by PK after membrane permeabilization.

(D) Western blot of pT71 Rab29 and total Rab29 from brain lysate, autophagosome fraction, and autophagosome fraction after treatment with PK.

(legend continued on next page)

Next, we investigated whether endogenous Rab29 and LRRK2 are present on AVs. We isolated AVs through sequential ultracentrifugation of mouse brain lysates (Figure S6D),[21,48] adding Gly-Phe-β-naphthylamide (GPN) to inactivate and deplete lysosomal vesicles. We detected total Rab29, LRRK2-phosphorylated pT71 Rab29, and LRRK2 in immunoblots of isolated AVs from WT or G2019S KI mice. Total Rab29, pT71 Rab29, and LRRK2 were all lost after treating isolated AVs with Proteinase K (Figures 5C, 5D, and S6E). This indicates that Rab29 and LRRK2 are bound to the outer AV membrane, corroborating the results of our Halo-Rab29 photobleaching experiments as well as previous reports of the recruitment of LRRK2 to autophagosomes.[47,49,50] Luminal proteins such as LC3-II were protected by the AV membrane from Proteinase K treatment and only degraded after membrane permeabilization by Triton X-100 (Figure S6E). The Golgi marker GM130 was not detected in the isolated AV fraction, excluding the possibility that Rab29 signal was due to contamination of isolated AVs with Golgi membrane (Figure S6E). Notably, pT71 Rab29, but not total Rab29, was enriched in the AV fraction compared with the total brain lysate input (Figure 5D). Consistent with higher LRRK2 kinase activity, we detected increased levels of pT71 Rab29 on AVs from G2019S KI mice (Figure 5E). There was no difference in the amount of total Rab29 or LRRK2 between WT and G2019S KI AVs (Figures 5F and S6F).

Rab29 overexpression disrupts axonal AV transport similar to G2019S mutation

In non-neuronal cells, overexpression of Rab29 has been shown to recruit LRRK2 to the membrane of the Golgi and increase LRRK2 kinase activity.[14,16] Recent studies found that membrane association, but not membrane identity, is important for LRRK2 activation by Rab29.[15,51]

Since we detected Rab29 on axonal AVs, we investigated whether overexpression of Rab29 affects the processivity of AV transport in a similar manner to the LRRK2-G2019S mutation. We transiently expressed EGFP-Rab29 and mCherry-LC3 in WT or G2019S KI mouse cortical neurons. EGFP-Rab5 was used as a negative control, since Rab5 is not known to affect LRRK2 kinase activity.[14] As expected, AVs in G2019S KI neurons overexpressing Rab5 paused more frequently than in WT neurons overexpressing Rab5 (Figures 5G and 5H). The pause frequency in WT neurons overexpressing Rab29 was significantly increased compared with WT neurons overexpressing Rab5, but similar to G2019S KI neurons overexpressing Rab5. Rab29 overexpression in G2019S KI neurons did not have an additive effect, but resulted in a pause number similar to either WT neurons overexpressing Rab29 or G2019S KI neurons overexpressing Rab5 (Figure 5H). While pause number was significantly increased, overexpression of Rab29 did not affect average pause duration (Figure S6G). Fraction of time paused and Δ run length were significantly increased; but again, overexpression of Rab29 did not produce an additive effect in G2019S KI neurons (Figures 5I and 5J). These observations are consistent with reports that LRRK2 and Rab29 act within the same pathway.[52,53]

LRRK2 kinase inhibition rescues AV transport in Rab29-overexpressing neurons

Next, we tested whether Rab29 overexpression affects AV transport through activation of LRRK2 kinase activity; if so, the LRRK2 kinase inhibitor MLi-2 should rescue defective transport in Rab29-overexpressing cells. While the comigration of axonal LC3 and Rab29 vesicles was not affected by MLi-2 (Figure S6H), LRRK2 kinase inhibition significantly reduced pause number, fraction of time paused, and Δ run length of axonal AVs in WT neurons expressing EGFP-Rab29 (Figures 5H–5J). All parameters were rescued to levels similar to WT neurons expressing Rab5 as a negative control. Consistent with earlier experiments, pause duration was not affected by MLi-2 (Figure S6G). Together, our data demonstrate that increased LRRK2 activity, caused by either the G2019S mutation or Rab29 overexpression, disrupts the processivity of axonal AV transport.

LRRK2-G2019S enhances recruitment of JIP4 to the AV membrane and increases kinesin activity

Both the anterograde motor kinesin and the retrograde motor dynein are bound to AVs; the opposing activities of these motors are regulated by adaptor proteins that inhibit kinesin and promote dynein activity.[21,43] The observed increases in reversals and non-processive motility suggest that LRRK2 hyperactivation may increase kinesin activity and thus disrupt AV transport by causing an unregulated tug of war between anterograde and retrograde motors.

JIP3 and JIP4 are motor adaptor proteins that bind LRRK2-phosphorylated Rab proteins: Rab8, Rab10, and Rab35.[11,12,51] In astrocytes, expression of LRRK2-G2019S increased recruitment of JIP4 to damaged lysosomes by enhancing Rab phosphorylation.[12] In line with these findings, we detected significantly higher levels of JIP4 on autophagosomes isolated from the brains of G2019S KI mice than WT mice (Figure 6A). JIP3 levels showed a similar trend, but did not reach statistical significance (Figure S7A). Both Rab8 and Rab10 were present on the outer AV membrane (Figure S7B). Western blots using a pan-specific pT Rab antibody (detecting JIP4-interacting phospho-Rab8, -Rab10, and -Rab35) showed enrichment of pT Rabs in the AV fraction and increased levels of LRRK2-phosphorylated Rab proteins on AVs from G2019S KI mice (Figure 6B).

(E and F) Western blot quantification of (E) pT71 Rab29 levels (mean ± SEM; n = 8–9 biological replicates; *p = 0.022; Mann-Whitney test) and (F) total Rab29 levels (mean ± SEM; n = 7–9 biological replicates; ns, not significant, p = 0.25; Mann-Whitney test) in autophagosome fraction of WT and G2019S KI mice. Data shown are normalized to total protein and relative to whole-brain lysate. Western blots of LRRK2, GM130, and LC3 are shown in Figures S6D–S6F.

(G) Kymographs of axonal EGFP-Rab5 or EGFP-Rab29 vesicles and mCherry-LC3 vesicles in mouse WT cortical neurons. Magenta arrowheads point to tracks of mCherry-LC3 vesicles; green arrowheads highlight EGFP-Rab29 tracks that colocalize with mCherry-LC3 tracks.

(H–J) Pause number (H), fraction of time paused (I), and Δ run length (J) of AVs in WT and G2019S KI neurons overexpressing Rab5 or Rab29 and in Rab29-overexpressing WT neurons treated with DMSO or MLi-2 (overexpression of Rab5 or Rab29: mean ± SEM; n = 107–149 AVs from 27 to 38 neurons from 3 to 4 independent cultures; ns, not significant, p > 0.06; **p < 0.001; ***p < 0.0001; Kruskal-Wallis with Dunn's multiple comparisons test). Treatment of Rab29-overexpressing neurons with DMSO or MLi-2 (mean ± SEM; n = 78–109 AVs from 26 to 27 neurons from 3 independent cultures; ns, not significant, p = 0.19; ***p < 0.0001; Mann-Whitney test). See also Figures S6G and S6H.

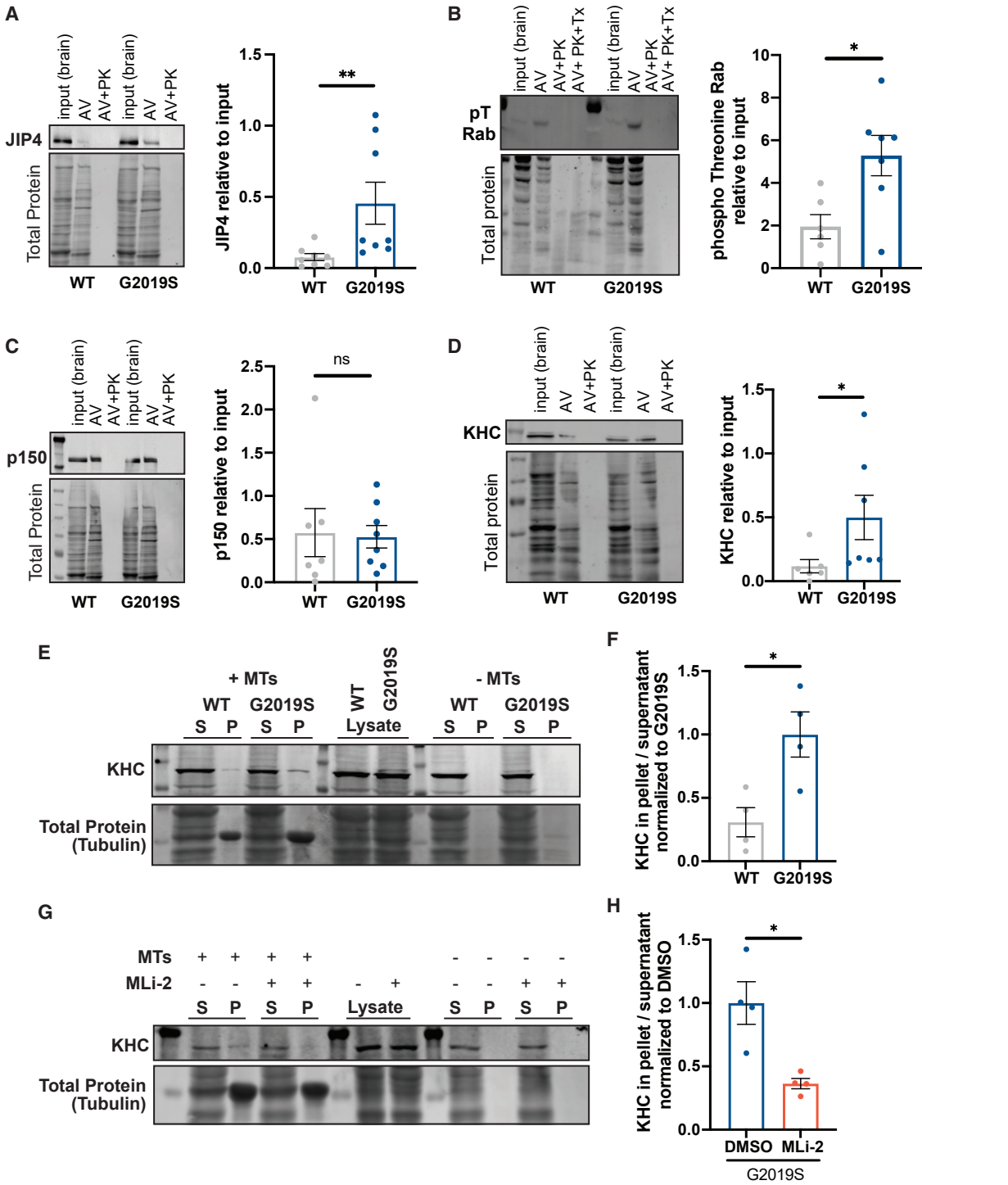

Figure 6. LRRK2-G2019S recruits JIP4 to the AV membrane and activates kinesin

(A–D) Representative western blot and quantification of (A) JIP4 (mean ± SEM; n = 8 biological replicates; **p = 0.0047; Mann-Whitney test); (B) phosphothreonine Rabs (mean ± SEM; n = 6–7 biological replicates; *p = 0.0135; Welch's t test); (C) p150^{Glued} (mean ± SEM; n = 7–8 biological replicates; *p = 0.61; Mann-Whitney test); and (D) KHC (mean ± SEM; n = 6–7 biological replicates; *p = 0.014; Mann-Whitney test) in the autophagosome fraction of WT and G2019S KI mouse brain lysates. Data shown are normalized to total protein and relative to whole-brain lysate.

(legend continued on next page)

LRRK2-phosphorylated pT73 Rab10, but not total Rab10, was enriched in the autophagosome fraction (Figure S7B).

JIP4 activates kinesin by binding kinesin light chain and kinesin heavy chain (KHC).[54,55] Binding of the GTPase Arf6 to the leucine zipper II domain of JIP4 interferes with JIP4's association with kinesin, but favors interaction with the dynein activator dynactin.[56,57] While JIP4 levels were increased on G2019S KI AVs, we detected only low levels of Arf6 associated with AVs and found no difference between Arf6 levels on WT and G2019S KI AVs (Figure S7C). Furthermore, levels of $p150^{Glued}$, a subunit of dynactin, were similar on WT and G2019S KI AVs (Figure 6C). In contrast and consistent with recruitment of kinesin by JIP4, KHC levels were significantly higher on G2019S KI AVs than on WT AVs (Figure 6D). The presence of JIP4, KHC, and $p150^{Glued}$ on axonal AVs in G2019S KI neurons was confirmed by immunofluorescence (IF) staining (Figures S7D and S7E). A microtubule-pelleting assay in the presence of adenylyl-imidodiphosphate (AMP-PNP; a non-hydrolysable ATP analog) showed increased microtubule binding of KHC from G2019S KI mouse embryonic fibroblast (MEF) lysates compared with WT, indicating that LRRK2 hyperactivation increases levels of activated kinesin (Figures 6E and 6F). Treatment with MLi-2 rescued this effect (Figures 6G and 6H). This suggests that by recruiting JIP4, hyperactive LRRK2 increases the amount of active kinesin on the autophagosomal membrane, resulting in a tug of war with the retrograde motor dynein that is predicted to induce more pausing and directional reversals, thus decreasing processive retrograde motility.

JIP4 overexpression disrupts axonal AV transport

To test whether increased JIP4 association interferes with processive axonal AV motility, we analyzed the transport of EGFP-LC3 vesicles in Halo-JIP4-overexpressing mouse WT neurons. We observed robust comigration of EGFP-LC3 and Halo-JIP4 vesicles (Figures 7A and 7B; Video S7). Strikingly, Halo-JIP4 overexpression was sufficient to increase the percentage of AVs moving either bidirectionally or in the anterograde direction while decreasing the fraction of retrograde AVs (Figure 7C), consistent with higher kinesin activity on AVs in JIP4-overexpressing neurons. Similar to the effect of G2019S mutation and Rab29 overexpression, JIP4 overexpression increased the number of pauses and time paused per minute of axonal AVs (Figures 7D and 7E). JIP4 overexpression also elevated the number of reversals and Δ run length during AV transport to levels about twice as high as in G2019S KI or Rab29 overexpressing neurons (Figures 7F and 7G). Thus, JIP4 overexpression resulted in a similar but more pronounced impairment of AV transport compared with the effects of LRRK2 hyperactivation. Overall, our findings support a model in which hyperactive LRRK2 recruits JIP4 to the AV membrane via its binding to LRRK2-phosphorylated Rab proteins. JIP4 then recruits and activates kinesin, resulting in a tug of war with the retrograde motor dynein and disruption of processive AV transport (Figures 7H and 7I).

DISCUSSION

There is a growing body of evidence linking dysfunctional autophagy to PD pathogenesis.[58,59] Previous reports support a role for LRRK2 as a regulator of autophagy and suggest that pathogenic LRRK2 mutations cause dysregulation of the autophagic pathway.[28–30,60–63] However, the underlying mechanism is not yet clear. The identification of a subgroup of Rab proteins as LRRK2 substrates links LRRK2 kinase activity to dynamic processes of intracellular trafficking and transport. Here, we used live imaging to study the effect of the most frequent pathogenic LRRK2 mutation, LRRK2-G2019S, on neuronal autophagy. We found that LRRK2-G2019S disrupts processive retrograde transport of axonal AVs in a kinase-dependent manner by increasing pause frequency and promoting non-processive motility. This effect was consistent across a LRRK2-G2019S overexpression model, primary G2019S KI neurons, and human G2019S KI iPSC-derived neurons.

Recent studies indicate that type 1 LRRK2 kinase inhibitors such as MLi-2 can promote binding of LRRK2 to microtubules and have raised the possibility that microtubule-bound LRRK2 may act as a roadblock for molecular motors.[41,64] However, at endogenous LRRK2 expression levels, MLi-2 does not appear to impair transport along microtubules. In fact, we found that MLi-2 improved the transport processivity of AVs in both G2019S KI and Rab29-overexpressing neurons, consistent with a beneficial effect of type 1 LRRK2 kinase inhibitors across multiple models of PD-related neurodegeneration.[65–67] We further found that neither treatment with MLi-2 nor expression of the G2019S mutation affected axonal microtubule dynamics.

In cell lines, overexpressed Rab29 recruits LRRK2 to the Golgi or to stressed lysosomes, leading to localized activation.[14,16,47,68,69] While membrane association is essential for LRRK2 activation by Rab29, specific membrane identity is not required.[15] We observed in neurons that EGFP-Rab29 robustly comigrated with axonal AVs and found endogenous Rab29 to be present on the outer membrane of isolated autophagosomes. Overexpression of EGFP-Rab29 in mouse WT neurons disrupted AV transport similar to expression of the G2019S mutation. Treatment with MLi-2 rescued AV processivity in Rab29-overexpressing neurons, confirming that Rab29 overexpression disrupts AV transport by increasing LRRK2 kinase activity. Rab29 overexpression in G2019S KI neurons did not have an additive effect, but resulted in a pause number similar to G2019S KI neurons without Rab29 overexpression and to WT neurons overexpressing Rab29. The non-additive effect of G2019S mutation and Rab29 overexpression suggests that both act within the same pathway and that reaching a certain threshold of LRRK2 activity causes the observed impairment of AV transport. Our result is in line with genetic studies showing that variants of LRRK2 and the Rab29-containing PARK16 locus do not increase PD risk in an additive manner.[70]

(E and F) Microtubule-pelleting assay (E) with lysates of WT or G2019S KI MEFs incubated with guanosine-5'-[(αβ)-methyleno]triphosphate (GMPCPP)-stabilized microtubules (5 μM) in the presence of 10 mM AMP-PNP and quantification (F) of KHC bound to the microtubule pellet (mean ± SEM; n = 4 biological replicates; *p = 0.0216; Welch's t test).

(G and H) Microtubule-pelleting assay (G) with lysates of G2019S KI MEFs treated with 200 nM MLi-2 overnight and quantification (H) of KHC bound to the microtubule pellet (mean ± SEM; n = 4 biological replicates; *p = 0.0286; Welch's t test). S, supernatant; P, pellet.

Figure S7 shows additional western blots and IF staining.

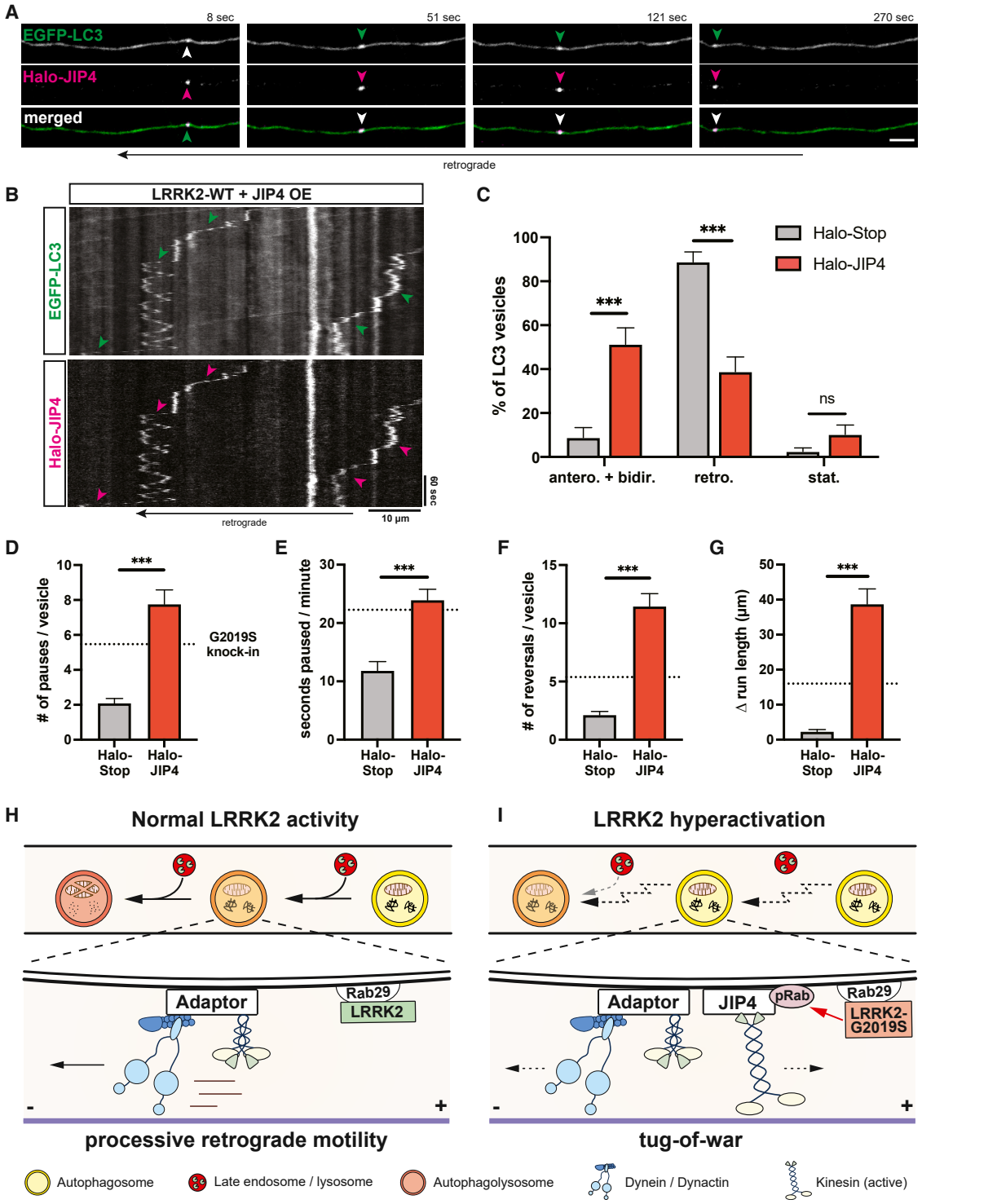

Figure 7. Overexpression of JIP4 disrupts AV transport

(A) Time-lapse images of axonal EGFP-LC3 and Halo-JIP4 vesicles in a mouse WT cortical neuron. Scale bar, 5 µm. See also Video S7.

(B) Kymographs of axonal EGFP-LC3 and Halo-JIP4 vesicles. Arrowheads highlight comigration.

(C) Directionality of EGFP-LC3 vesicles in Halo-Tag-only and Halo-JIP4-overexpressing WT neurons (mean ± SEM; n = 24–25 neurons from 3 independent cultures; ***$p < 0.0001$; two-way ANOVA). Antero + bidir., anterograde + bidirectional; retro., retrograde; stat., stationary.

(D–G) Pause number (D), fraction of time paused (E), number of reversals (F), and Δ run length (G) of AVs in Halo-Tag-only and Halo-JIP4-overexpressing neurons (mean ± SEM; n = 68–87 AVs from 24 to 25 neurons from 3 independent cultures; ***$p < 0.0001$; Mann-Whitney test). Dotted lines indicate the respective average observed in mouse G2019S KI neurons.

(legend continued on next page)

How does increased LRRK2 activity mediate the observed disruption of AV transport by LRRK2-G2019S or Rab29 overexpression? Physiologically, the scaffold proteins huntingtin, huntingtin-associated protein 1 (HAP1), and JIP1 (structurally distinct from JIP4) enable processive retrograde AV transport by inhibiting kinesin and promoting dynein activity (Figure 7H).[25,43] AVs from G2019S KI mice have increased levels of phospho-Rabs and JIP4, a motor adaptor protein that has been shown to bind to LRRK2-phosphorylated Rab proteins.[11,12] JIP4 recruits and activates the anterograde motor kinesin, unless kinesin binding is competitively blocked by the GTPase Arf6.[57] We observed that increased levels of JIP4 on G2019S AVs were accompanied by increased levels of kinesin and that increasing JIP4 levels by overexpression was sufficient to induce a significantly higher fraction of anterogradely and bidirectionally moving AVs in live-imaging experiments. These results support a model in which hyperactive LRRK2 recruits JIP4 to the AV membrane via its binding to LRRK2-phosphorylated Rab proteins. JIP4 then recruits and activates kinesin, resulting in a tug of war with the retrograde motor dynein that is activated by other AV-resident motor adaptors (Figure 7I). Further work is required to determine which specific phospho-Rab(s) mediate recruitment of JIP4 to the AV membrane. The described model is supported by the phenotype observed in our live-imaging experiments, where LRRK2 activation by G2019S mutation or Rab29 overexpression caused an increase in reversals and non-processive AV motility.

By contrast, we did not detect an effect of LRRK2-G2019S on the axonal transport of LAMP1 vesicles. This is somewhat surprising, as previous reports have found LRRK2-mediated recruitment of JIP4 to the membrane of LAMP1 vesicles in non-neuronal cells.[12] Notably, motility of axonal LAMP1 vesicles is overall less processive than transport of AVs (LAMP1 vesicles: ~50% bidirectional/stationary, 25% anterograde, 25% retrograde; AVs: ~80% retrograde vesicles).[34,42,71,72] Thus, it is possible that JIP4 recruitment by hyperactive LRRK2 only results in a measurable effect for AVs, where increased JIP4 levels disrupt mechanisms that normally ensure robust retrograde AV motility. Alternatively, the related kinase LRRK1, rather than LRRK2, may play a role in controlling the retrograde motility of LAMP1-positive late endosomes/lysosomes. The late endosome marker Rab7 is phosphorylated by LRRK1, but not LRRK2, at S72.[73] Rab7 phosphorylation by LRRK1 has been implicated in mediating the recruitment of Rab7-interacting lysosomal protein (RILP),[74] a scaffold protein that promotes retrograde transport of late endosomes/lysosomes by enhancing dynein activity.[75]

Previous work has shown that efficient autophagosomal cargo degradation is dependent on functional retrograde transport.[76] Disruption of retrograde axonal AV transport in a model of Huntington's disease caused ineffective autophagosome-lysosome fusion and impaired autophagosomal cargo degradation.[25] Knockdown of the motor scaffold protein JIP1 was also sufficient to disrupt retrograde AV transport and reduce acidification.[43] Similarly, we found that disrupted transport in G2019S KI axons was accompanied by a defect in AV acidification. While we observed no change in density, transport, or acidification of axonal LAMP1 vesicles in G2019S neurons, we cannot fully exclude the potential contribution of lysosomal defects to impaired AV maturation. In line with our results, overexpression of LRRK2-G2019S in rat neurons decreased autophagic flux, but did not affect lysosomal pH.[30] Disruption of transport and ineffective acidification may delay autophagosomal cargo degradation and over time result in buildup of protein aggregates and/or dysfunctional organelles in the axon. Indeed, accumulation of alpha-synuclein aggregates in the axon ("Lewy neurites") has been shown to occur early during PD pathogenesis.[77–79] Evidence from human histopathology and animal models suggests that axonal pathology precedes damage to the neuronal cell body in PD, supporting a "retrograde axonal degeneration" disease model.[80–82]

In summary, our work robustly links dysregulation of the LRRK2 pathway to defects in neuronal AV transport. We show across different model systems that increased LRRK2 kinase activity induced by either G2019S mutation or Rab29 overexpression strikingly disrupts the processivity of axonal AV transport. Mechanistically, we found that LRRK2 hyperactivation recruits JIP4 to the AV membrane, activating kinesin and resulting in a tug of war between anterograde and retrograde motors. Our data connect dysfunction of LRRK2, a kinase that affects intracellular trafficking by phosphorylating Rab proteins, with defects in autophagy, a pathway that has long been implicated in the pathogenesis of PD.

STAR★METHODS

Detailed methods are provided in the online version of this paper and include the following:

- KEY RESOURCES TABLE
- RESOURCE AVAILABILITY
  - Lead contact
  - Materials availability
  - Data and code availability
- EXPERIMENTAL MODEL AND SUBJECT DETAILS
  - Primary neuron culture
  - Human iPSC culture and neuronal differentiation
- METHOD DETAILS
  - Plasmids
  - Generation of LRRK2-G2019S knockin iPSCs
  - Live-cell imaging
  - Autophagosome isolation assay
  - Microtubule pelleting assay
  - Immunoblotting
  - Immunostaining
- QUANTIFICATION AND STATISTICAL ANALYSIS

(H and I) Model depicting the effect of increased LRRK2 kinase activity on axonal AV transport and maturation. (H) Normal LRRK2 activity allows for processive retrograde AV transport, facilitating efficient fusion *en route* with lysosomal vesicles. Motor adaptors inhibit kinesin and promote dynein activity, resulting in processive retrograde transport. (I) LRRK2 hyperactivation by LRRK2-G2019S mutation or Rab29 overexpression disrupts processive AV transport, leading to inefficient autophagosome-lysosome fusion and impaired AV acidification. Hyperactive LRRK2 enhances recruitment of JIP4 to the AV membrane via binding to phospho-Rabs, resulting in abnormal kinesin activation and a tug of war between anterograde and retrograde motors.

- LC3 and LAMP1 vesicle motility
- EB3 dynamics
- Autophagosome acidification (mCherry-EGFP-LC3 tandem construct)
- Late endosome/lysosome acidification (SEP-LAMP1-RFP construct)
- Rab29 FRAP assay
- Statistical analysis

SUPPLEMENTAL INFORMATION

Supplemental information can be found online at https://doi.org/10.1016/j.cub.2021.02.061.

ACKNOWLEDGMENTS

We thank Andrea Stavoe and Cameron Thompson for sharing their initial observations on LRRK2 and autophagy. We thank Mariko Tokito for assistance in the cloning of plasmid constructs; Jean Ann Maguire and the staff of the Human Pluripotent Stem Cell Core at the Children's Hospital of Philadelphia for expertise in the generation of CRISPR KI iPSCs; and Shalini Padmanabhan (Michael J. Fox Foundation) for helpful discussions. This work was supported by the German Research Foundation (DFG; BO 5434/1-1 to C.A.B.), the National Institutes of Health (R37 NS060698 to E.L.F.H.), and the Michael J. Fox Foundation (grant 15100 to E.L.F.H.).

AUTHOR CONTRIBUTIONS

Conceptualization, C.A.B. and E.L.F.H.; methodology, C.A.B. and J.G.; investigation, C.A.B., J.G., D.D., and G.G.C.; writing—original draft, C.A.B. and E.L.F.H.; writing—review and editing, C.A.B., J.G., D.D., and E.L.F.H.; funding acquisition, C.A.B. and E.L.F.H.; supervision, E.L.F.H.

DECLARATION OF INTERESTS

The authors declare no competing interests.

Received: July 21, 2020
Revised: December 14, 2020
Accepted: February 26, 2021
Published: March 24, 2021

REFERENCES

1. Zimprich, A., Biskup, S., Leitner, P., Lichtner, P., Farrer, M., Lincoln, S., Kachergus, J., Hulihan, M., Uitti, R.J., Calne, D.B., et al. (2004). Mutations in LRRK2 cause autosomal-dominant parkinsonism with pleomorphic pathology. Neuron *44*, 601–607.
2. Healy, D.G., Falchi, M., O'Sullivan, S.S., Bonifati, V., Durr, A., Bressman, S., Brice, A., Aasly, J., Zabetian, C.P., Goldwurm, S., et al.; International LRRK2 Consortium (2008). Phenotype, genotype, and worldwide genetic penetrance of LRRK2-associated Parkinson's disease: a case-control study. Lancet Neurol. *7*, 583–590.
3. West, A.B., Moore, D.J., Biskup, S., Bugayenko, A., Smith, W.W., Ross, C.A., Dawson, V.L., and Dawson, T.M. (2005). Parkinson's disease-associated mutations in leucine-rich repeat kinase 2 augment kinase activity. Proc. Natl. Acad. Sci. USA *102*, 16842–16847.
4. Smith, W.W., Pei, Z., Jiang, H., Dawson, V.L., Dawson, T.M., and Ross, C.A. (2006). Kinase activity of mutant LRRK2 mediates neuronal toxicity. Nat. Neurosci. *9*, 1231–1233.
5. Greggio, E., Jain, S., Kingsbury, A., Bandopadhyay, R., Lewis, P., Kaganovich, A., van der Brug, M.P., Beilina, A., Blackinton, J., Thomas, K.J., et al. (2006). Kinase activity is required for the toxic effects of mutant LRRK2/dardarin. Neurobiol. Dis. *23*, 329–341.
6. Mir, R., Tonelli, F., Lis, P., Macartney, T., Polinski, N.K., Martinez, T.N., Chou, M.-Y., Howden, A.J.M., König, T., Hotzy, C., et al. (2018). The Parkinson's disease VPS35[D620N] mutation enhances LRRK2-mediated Rab protein phosphorylation in mouse and human. Biochem. J. *475*, 1861–1883.
7. Di Maio, R., Hoffman, E.K., Rocha, E.M., Keeney, M.T., Sanders, L.H., De Miranda, B.R., Zharikov, A., Van Laar, A., Stepan, A.F., Lanz, T.A., et al. (2018). LRRK2 activation in idiopathic Parkinson's disease. Sci. Transl. Med. *10*, 1–13.
8. Steger, M., Tonelli, F., Ito, G., Davies, P., Trost, M., Vetter, M., Wachter, S., Lorentzen, E., Duddy, G., Wilson, S., et al. (2016). Phosphoproteomics reveals that Parkinson's disease kinase LRRK2 regulates a subset of Rab GTPases. eLife *5*, 1–28.
9. Steger, M., Diez, F., Dhekne, H.S., Lis, P., Nirujogi, R.S., Karayel, O., Tonelli, F., Martinez, T.N., Lorentzen, E., Pfeffer, S.R., et al. (2017). Systematic proteomic analysis of LRRK2-mediated Rab GTPase phosphorylation establishes a connection to ciliogenesis. eLife *6*, 1–22.
10. Kiral, F.R., Kohrs, F.E., Jin, E.J., and Hiesinger, P.R. (2018). Rab GTPases and Membrane Trafficking in Neurodegeneration. Curr. Biol. *28*, R471–R486.
11. Waschbüsch, D., Purlyte, E., Pal, P., McGrath, E., Alessi, D.R., and Khan, A.R. (2020). Structural Basis for Rab8a Recruitment of RILPL2 via LRRK2 Phosphorylation of Switch 2. Structure *28*, 406–417.e6.
12. Bonet-Ponce, L., Beilina, A., Williamson, C.D., Lindberg, E., Kluss, J.H., Saez-Atienzar, S., Landeck, N., Kumaran, R., Mamais, A., Bleck, C.K.E., et al. (2020). LRRK2 mediates tubulation and vesicle sorting from lysosomes. Sci. Adv. *6*, 1–16.
13. Simón-Sánchez, J., Schulte, C., Bras, J.M., Sharma, M., Gibbs, J.R., Berg, D., Paisan-Ruiz, C., Lichtner, P., Scholz, S.W., Hernandez, D.G., et al. (2009). Genome-wide association study reveals genetic risk underlying Parkinson's disease. Nat. Genet. *41*, 1308–1312.
14. Purlyte, E., Dhekne, H.S., Sarhan, A.R., Gomez, R., Lis, P., Wightman, M., Martinez, T.N., Tonelli, F., Pfeffer, S.R., and Alessi, D.R. (2018). Rab29 activation of the Parkinson's disease-associated LRRK2 kinase. EMBO J. *37*, 1–18.
15. Gomez, R.C., Wawro, P., Lis, P., Alessi, D.R., and Pfeffer, S.R. (2019). Membrane association but not identity is required for LRRK2 activation and phosphorylation of Rab GTPases. J. Cell Biol. *218*, 4157–4170.
16. Liu, Z., Bryant, N., Kumaran, R., Beilina, A., Abeliovich, A., Cookson, M.R., and West, A.B. (2018). LRRK2 phosphorylates membrane-bound Rabs and is activated by GTP-bound Rab7L1 to promote recruitment to the trans-Golgi network. Hum. Mol. Genet. *27*, 385–395.
17. Guedes-Dias, P., and Holzbaur, E.L.F. (2019). Axonal transport: Driving synaptic function. Science *366*, eaaw9997.
18. Matsuda, W., Furuta, T., Nakamura, K.C., Hioki, H., Fujiyama, F., Arai, R., and Kaneko, T. (2009). Single nigrostriatal dopaminergic neurons form widely spread and highly dense axonal arborizations in the neostriatum. J. Neurosci. *29*, 444–453.
19. Giguère, N., Burke Nanni, S., and Trudeau, L.-E. (2018). On Cell Loss and Selective Vulnerability of Neuronal Populations in Parkinson's Disease. Front. Neurol. *9*, 455.
20. Stavoe, A.K.H., and Holzbaur, E.L.F. (2019). Autophagy in Neurons. Annu. Rev. Cell Dev. Biol. *35*, 477–500.
21. Maday, S., Wallace, K.E., and Holzbaur, E.L.F. (2012). Autophagosomes initiate distally and mature during transport toward the cell soma in primary neurons. J. Cell Biol. *196*, 407–417.
22. Maday, S., and Holzbaur, E.L.F. (2014). Autophagosome biogenesis in primary neurons follows an ordered and spatially regulated pathway. Dev. Cell *30*, 71–85.
23. Stavoe, A.K.H., Hill, S.E., Hall, D.H., and Colón-Ramos, D.A. (2016). KIF1A/UNC-104 Transports ATG-9 to Regulate Neurodevelopment and Autophagy at Synapses. Dev. Cell *38*, 171–185.

24. Neisch, A.L., Neufeld, T.P., and Hays, T.S. (2017). A STRIPAK complex mediates axonal transport of autophagosomes and dense core vesicles through PP2A regulation. J. Cell Biol. *216*, 441–461.

25. Wong, Y.C., and Holzbaur, E.L.F. (2014). The regulation of autophagosome dynamics by huntingtin and HAP1 is disrupted by expression of mutant huntingtin, leading to defective cargo degradation. J. Neurosci. *34*, 1293–1305.

26. Yue, M., Hinkle, K.M., Davies, P., Trushina, E., Fiesel, F.C., Christenson, T.A., Schroeder, A.S., Zhang, L., Bowles, E., Behrouz, B., et al. (2015). Progressive dopaminergic alterations and mitochondrial abnormalities in LRRK2 G2019S knock-in mice. Neurobiol. Dis. *78*, 172–195.

27. Schapansky, J., Khasnavis, S., DeAndrade, M.P., Nardozzi, J.D., Falkson, S.R., Boyd, J.D., Sanderson, J.B., Bartels, T., Melrose, H.L., and LaVoie, M.J. (2018). Familial knockin mutation of LRRK2 causes lysosomal dysfunction and accumulation of endogenous insoluble α-synuclein in neurons. Neurobiol. Dis. *111*, 26–35.

28. Ramonet, D., Daher, J.P.L., Lin, B.M., Stafa, K., Kim, J., Banerjee, R., Westerlund, M., Pletnikova, O., Glauser, L., Yang, L., et al. (2011). Dopaminergic neuronal loss, reduced neurite complexity and autophagic abnormalities in transgenic mice expressing G2019S mutant LRRK2. PLoS ONE *6*, e18568.

29. Albanese, F., Novello, S., and Morari, M. (2019). Autophagy and LRRK2 in the Aging Brain. Front. Neurosci. *13*, 1352.

30. Wallings, R., Connor-Robson, N., and Wade-Martins, R. (2019). LRRK2 interacts with the vacuolar-type H+-ATPase pump a1 subunit to regulate lysosomal function. Hum. Mol. Genet. *28*, 2696–2710.

31. Matikainen-Ankney, B.A., Kezunovic, N., Mesias, R.E., Tian, Y., Williams, F.M., Huntley, G.W., and Benson, D.L. (2016). Altered Development of Synapse Structure and Function in Striatum Caused by Parkinson's Disease-Linked LRRK2-G2019S Mutation. J. Neurosci. *36*, 7128–7141.

32. Lis, P., Burel, S., Steger, M., Mann, M., Brown, F., Diez, F., Tonelli, F., Holton, J.L., Ho, P.W., Ho, S.-L., et al. (2018). Development of phospho-specific Rab protein antibodies to monitor *in vivo* activity of the LRRK2 Parkinson's disease kinase. Biochem. J. *475*, 1–22.

33. Maday, S., and Holzbaur, E.L.F. (2016). Compartment-Specific Regulation of Autophagy in Primary Neurons. J. Neurosci. *36*, 5933–5945.

34. Boecker, C.A., Olenick, M.A., Gallagher, E.R., Ward, M.E., and Holzbaur, E.L.F. (2020). ToolBox: Live Imaging of intracellular organelle transport in induced pluripotent stem cell-derived neurons. Traffic *21*, 138–155.

35. Fell, M.J., Mirescu, C., Basu, K., Cheewatrakoolpong, B., DeMong, D.E., Ellis, J.M., Hyde, L.A., Lin, Y., Markgraf, C.G., Mei, H., et al. (2015). MLi-2, a Potent, Selective, and Centrally Active Compound for Exploring the Therapeutic Potential and Safety of LRRK2 Kinase Inhibition. J. Pharmacol. Exp. Ther. *355*, 397–409.

36. Fernandopulle, M.S., Prestil, R., Grunseich, C., Wang, C., Gan, L., and Ward, M.E. (2018). Transcription Factor-Mediated Differentiation of Human iPSCs into Neurons. Curr. Protoc. Cell Biol. *79*, e51.

37. Bieri, G., Brahic, M., Bousset, L., Couthouis, J., Kramer, N.J., Ma, R., Nakayama, L., Monbureau, M., Defensor, E., Schüle, B., et al. (2019). LRRK2 modifies α-syn pathology and spread in mouse models and human neurons. Acta Neuropathol. *137*, 961–980.

38. Kett, L.R., Boassa, D., Ho, C.C.Y., Rideout, H.J., Hu, J., Terada, M., Ellisman, M., and Dauer, W.T. (2012). LRRK2 Parkinson disease mutations enhance its microtubule association. Hum. Mol. Genet. *21*, 890–899.

39. Law, B.M.H., Spain, V.A., Leinster, V.H.L., Chia, R., Beilina, A., Cho, H.J., Taymans, J.M., Urban, M.K., Sancho, R.M., Blanca Ramírez, M., et al. (2014). A direct interaction between leucine-rich repeat kinase 2 and specific β-tubulin isoforms regulates tubulin acetylation. J. Biol. Chem. *289*, 895–908.

40. Gillardon, F. (2009). Leucine-rich repeat kinase 2 phosphorylates brain tubulin-beta isoforms and modulates microtubule stability–a point of convergence in parkinsonian neurodegeneration? J. Neurochem. *110*, 1514–1522.

41. Deniston, C.K., Salogiannis, J., Mathea, S., Snead, D.M., Lahiri, I., Matyszewski, M., Donosa, O., Watanabe, R., Böhning, J., Shiau, A.K., et al. (2020). Structure of LRRK2 in Parkinson's disease and model for microtubule interaction. Nature *588*, 344–349.

42. Moughamian, A.J., and Holzbaur, E.L.F. (2012). Dynactin is required for transport initiation from the distal axon. Neuron *74*, 331–343.

43. Fu, M.M., Nirschl, J.J., and Holzbaur, E.L.F. (2014). LC3 binding to the scaffolding protein JIP1 regulates processive dynein-driven transport of autophagosomes. Dev. Cell *29*, 577–590.

44. Stavoe, A.K., Gopal, P.P., Gubas, A., Tooze, S.A., and Holzbaur, E.L. (2019). Expression of WIPI2B counteracts age-related decline in autophagosome biogenesis in neurons. eLife *8*, 1–36.

45. Evans, C.S., and Holzbaur, E.L. (2020). Degradation of engulfed mitochondria is rate-limiting in Optineurin-mediated mitophagy in neurons. eLife *9*, 1–30.

46. Farías, G.G., Guardia, C.M., De Pace, R., Britt, D.J., and Bonifacino, J.S. (2017). BORC/kinesin-1 ensemble drives polarized transport of lysosomes into the axon. Proc. Natl. Acad. Sci. USA *114*, E2955–E2964.

47. Eguchi, T., Kuwahara, T., Sakurai, M., Komori, T., Fujimoto, T., Ito, G., Yoshimura, S.I., Harada, A., Fukuda, M., Koike, M., and Iwatsubo, T. (2018). LRRK2 and its substrate Rab GTPases are sequentially targeted onto stressed lysosomes and maintain their homeostasis. Proc. Natl. Acad. Sci. USA *115*, E9115–E9124.

48. Strømhaug, P.E., Berg, T.O., Fengsrud, M., and Seglen, P.O. (1998). Purification and characterization of autophagosomes from rat hepatocytes. Biochem. J. *335*, 217–224.

49. Alegre-Abarrategui, J., Christian, H., Lufino, M.M.P., Mutihac, R., Venda, L.L., Ansorge, O., and Wade-Martins, R. (2009). LRRK2 regulates autophagic activity and localizes to specific membrane microdomains in a novel human genomic reporter cellular model. Hum. Mol. Genet. *18*, 4022–4034.

50. Schapansky, J., Nardozzi, J.D., Felizia, F., and LaVoie, M.J. (2014). Membrane recruitment of endogenous LRRK2 precedes its potent regulation of autophagy. Hum. Mol. Genet. *23*, 4201–4214.

51. Kluss, J.H., Beilina, A., Lewis, P.A., Cookson, M.R., and Bonet-Ponce, L. (2020). Membrane targeting activates Leucine-rich repeat kinase 2 with differential effects on downstream Rab activation. bioRxiv. https://doi.org/10.1101/2020.12.01.406223.

52. Kuwahara, T., Inoue, K., D'Agati, V.D., Fujimoto, T., Eguchi, T., Saha, S., Wolozin, B., Iwatsubo, T., and Abeliovich, A. (2016). LRRK2 and RAB7L1 coordinately regulate axonal morphology and lysosome integrity in diverse cellular contexts. Sci. Rep. *6*, 29945.

53. Mazza, M.C., Nguyen, V., Beilina, A., Ding, J., and Cookson, M.R. (2021). Combined knockout of Lrrk2 and Rab29 does not result in behavioral abnormalities in vivo. J. Parkinsons Dis. https://doi.org/10.3233/JPD-202172.

54. Watt, D., Dixit, R., and Cavalli, V. (2015). JIP3 activates kinesin-1 motility to promote axon elongation. J. Biol. Chem. *290*, 15512–15525.

55. Vilela, F., Velours, C., Chenon, M., Aumont-Nicaise, M., Campanacci, V., Thureau, A., Pylypenko, O., Andreani, J., Llinas, P., and Ménétrey, J. (2019). Structural characterization of the RH1-LZI tandem of JIP3/4 highlights RH1 domains as a cytoskeletal motor-binding motif. Sci. Rep. *9*, 16036.

56. Cockburn, J.J.B., Hesketh, S.J., Mulhair, P., Thomsen, M., O'Connell, M.J., and Way, M. (2018). Insights into Kinesin-1 Activation from the Crystal Structure of KLC2 Bound to JIP3. Structure *26*, 1486–1498.e6.

57. Montagnac, G., Sibarita, J.B., Loubéry, S., Daviet, L., Romao, M., Raposo, G., and Chavrier, P. (2009). ARF6 Interacts with JIP4 to control a motor switch mechanism regulating endosome traffic in cytokinesis. Curr. Biol. *19*, 184–195.

58. Lynch-Day, M.A., Mao, K., Wang, K., Zhao, M., and Klionsky, D.J. (2012). The role of autophagy in Parkinson's disease. Cold Spring Harb. Perspect. Med. *2*, a009357.

59. Anglade, P., Vyas, S., Javoy-Agid, F., Herrero, M.T., Michel, P.P., Marquez, J., Mouatt-Prigent, A., Ruberg, M., Hirsch, E.C., and Agid, Y. (1997). Apoptosis and autophagy in nigral neurons of patients with Parkinson's disease. Histol. Histopathol. *12*, 25–31.

60. Tong, Y., Yamaguchi, H., Giaime, E., Boyle, S., Kopan, R., Kelleher, R.J., 3rd, and Shen, J. (2010). Loss of leucine-rich repeat kinase 2 causes impairment of protein degradation pathways, accumulation of alpha-synuclein, and apoptotic cell death in aged mice. Proc. Natl. Acad. Sci. USA *107*, 9879–9884.

61. Giaime, E., Tong, Y., Wagner, L.K., Yuan, Y., Huang, G., and Shen, J. (2017). Age-Dependent Dopaminergic Neurodegeneration and Impairment of the Autophagy-Lysosomal Pathway in LRRK-Deficient Mice. Neuron *96*, 796–807.e6.

62. Sánchez-Danés, A., Richaud-Patin, Y., Carballo-Carbajal, I., Jiménez-Delgado, S., Caig, C., Mora, S., Di Guglielmo, C., Ezquerra, M., Patel, B., Giralt, A., et al. (2012). Disease-specific phenotypes in dopamine neurons from human iPS-based models of genetic and sporadic Parkinson's disease. EMBO Mol. Med. *4*, 380–395.

63. Plowey, E.D., Cherra, S.J., 3rd, Liu, Y.J., and Chu, C.T. (2008). Role of autophagy in G2019S-LRRK2-associated neurite shortening in differentiated SH-SY5Y cells. J. Neurochem. *105*, 1048–1056.

64. Watanabe, R., Buschauer, R., Böhning, J., Audagnotto, M., Lasker, K., Lu, T.W., Boassa, D., Taylor, S., and Villa, E. (2020). The In Situ Structure of Parkinson's Disease-Linked LRRK2. Cell *182*, 1508–1518.e16.

65. Daher, J.P.L., Abdelmotilib, H.A., Hu, X., Volpicelli-Daley, L.A., Moehle, M.S., Fraser, K.B., Needle, E., Chen, Y., Steyn, S.J., Galatsis, P., et al. (2015). Leucine-rich repeat kinase 2 (LRRK2) pharmacological inhibition abates α-synuclein gene-induced neurodegeneration. J. Biol. Chem. *290*, 19433–19444.

66. Volpicelli-Daley, L.A., Abdelmotilib, H., Liu, Z., Stoyka, L., Daher, J.P.L., Milnerwood, A.J., Unni, V.K., Hirst, W.D., Yue, Z., Zhao, H.T., et al. (2016). G2019S-LRRK2 expression augments α-synuclein sequestration into inclusions in neurons. J. Neurosci. *36*, 7415–7427.

67. Yao, C., Johnson, W.M., Gao, Y., Wang, W., Zhang, J., Deak, M., Alessi, D.R., Zhu, X., Mieyal, J.J., Roder, H., et al. (2013). Kinase inhibitors arrest neurodegeneration in cell and C. elegans models of LRRK2 toxicity. Hum. Mol. Genet. *22*, 328–344.

68. Beilina, A., Rudenko, I.N., Kaganovich, A., Civiero, L., Chau, H., Kalia, S.K., Kalia, L.V., Lobbestael, E., Chia, R., Ndukwe, K., et al.; International Parkinson's Disease Genomics Consortium; North American Brain Expression Consortium (2014). Unbiased screen for interactors of leucine-rich repeat kinase 2 supports a common pathway for sporadic and familial Parkinson disease. Proc. Natl. Acad. Sci. USA *111*, 2626–2631.

69. Madero-Pérez, J., Fernández, B., Lara Ordóñez, A.J., Fdez, E., Lobbestael, E., Baekelandt, V., and Hilfiker, S. (2018). RAB7L1-mediated relocalization of LRRK2 to the golgi complex causes centrosomal deficits via RAB8A. Front. Mol. Neurosci. *11*, 417.

70. Pihlstrøm, L., Rengmark, A., Bjørnarå, K.A., Dizdar, N., Fardell, C., Forsgren, L., Holmberg, B., Larsen, J.P., Linder, J., Nissbrandt, H., et al. (2015). Fine mapping and resequencing of the PARK16 locus in Parkinson's disease. J. Hum. Genet. *60*, 357–362.

71. Maday, S., Twelvetrees, A.E., Moughamian, A.J., and Holzbaur, E.L.F. (2014). Axonal transport: cargo-specific mechanisms of motility and regulation. Neuron *84*, 292–309.

72. Hendricks, A.G., Perlson, E., Ross, J.L., Schroeder, H.W., 3rd, Tokito, M., and Holzbaur, E.L.F. (2010). Motor coordination via a tug-of-war mechanism drives bidirectional vesicle transport. Curr. Biol. *20*, 697–702.

73. Malik, A.U., Karapetsas, A., Nirujogi, R.S., Mathea, S., Pal, P., Lis, P., Taylor, M., Purlyte, E., Gourlay, R., Dorward, M., et al. (2020). Deciphering the LRRK code: LRRK1 and LRRK2 phosphorylate distinct Rab proteins and are regulated by diverse mechanisms. bioRxiv. https://doi.org/10.1101/2020.11.25.397836.

74. Hanafusa, H., Yagi, T., Ikeda, H., Hisamoto, N., Nishioka, T., Kaibuchi, K., Shirakabe, K., and Matsumoto, K. (2019). LRRK1 phosphorylation of Rab7 at S72 links trafficking of EGFR-containing endosomes to its effector RILP. J. Cell Sci. *132*, jcs228809.

75. Jordens, I., Fernandez-Borja, M., Marsman, M., Dusseljee, S., Janssen, L., Calafat, J., Janssen, H., Wubbolts, R., and Neefjes, J. (2001). The Rab7 effector protein RILP controls lysosomal transport by inducing the recruitment of dynein-dynactin motors. Curr. Biol. *11*, 1680–1685.

76. Ravikumar, B., Acevedo-Arozena, A., Imarisio, S., Berger, Z., Vacher, C., O'Kane, C.J., Brown, S.D.M., and Rubinsztein, D.C. (2005). Dynein mutations impair autophagic clearance of aggregate-prone proteins. Nat. Genet. *37*, 771–776.

77. Braak, H., Del Tredici, K., Rüb, U., de Vos, R.A.I., Jansen Steur, E.N.H., and Braak, E. (2003). Staging of brain pathology related to sporadic Parkinson's disease. Neurobiol. Aging *24*, 197–211.

78. Volpicelli-Daley, L.A., Luk, K.C., Patel, T.P., Tanik, S.A., Riddle, D.M., Stieber, A., Meaney, D.F., Trojanowski, J.Q., and Lee, V.M.Y. (2011). Exogenous α-synuclein fibrils induce Lewy body pathology leading to synaptic dysfunction and neuron death. Neuron *72*, 57–71.

79. Lingor, P., Koch, J.C., Tönges, L., and Bähr, M. (2012). Axonal degeneration as a therapeutic target in the CNS. Cell Tissue Res. *349*, 289–311.

80. Chung, C.Y., Koprich, J.B., Siddiqi, H., and Isacson, O. (2009). Dynamic changes in presynaptic and axonal transport proteins combined with striatal neuroinflammation precede dopaminergic neuronal loss in a rat model of AAV α-synucleinopathy. J. Neurosci. *29*, 3365–3373.

81. Tagliaferro, P., and Burke, R.E. (2016). Retrograde Axonal Degeneration in Parkinson Disease. J. Parkinsons Dis. *6*, 1–15.

82. Burke, R.E., and O'Malley, K. (2013). Axon degeneration in Parkinson's disease. Exp. Neurol. *246*, 72–83.

83. Wang, C., Ward, M.E., Chen, R., Liu, K., Tracy, T.E., Chen, X., Xie, M., Sohn, P.D., Ludwig, C., Meyer-Franke, A., et al. (2017). Scalable Production of iPSC-Derived Human Neurons to Identify Tau-Lowering Compounds by High-Content Screening. Stem Cell Reports *9*, 1221–1233.

84. Maguire, J.A., Cardenas-Diaz, F.L., Gadue, P., and French, D.L. (2019). Highly Efficient CRISPR-Cas9-Mediated Genome Editing in Human Pluripotent Stem Cells. Curr. Protoc. Stem Cell Biol. *48*, e64.

85. Kaech, S., and Banker, G. (2006). Culturing hippocampal neurons. Nat. Protoc. *1*, 2406–2415.

86. Guedes-Dias, P., Nirschl, J.J., Abreu, N., Tokito, M.K., Janke, C., Magiera, M.M., and Holzbaur, E.L.F. (2019). Kinesin-3 Responds to Local Microtubule Dynamics to Target Synaptic Cargo Delivery to the Presynapse. Curr. Biol. *29*, 268–282.e8.

87. Mangeol, P., Prevo, B., and Peterman, E.J.G. (2016). KymographClear and KymographDirect: two tools for the automated quantitative analysis of molecular and cellular dynamics using kymographs. Mol. Biol. Cell *27*, 1948–1957.

STAR★METHODS

KEY RESOURCES TABLE

REAGENT or RESOURCE	SOURCE	IDENTIFIER
Antibodies		
Anti-LRRK2, Rabbit Monoclonal	Abcam	Cat# ab133474; RRID: AB_2713963
Anti-Rab29, Rabbit Monoclonal	Abcam	Cat# ab256526; RRID: AB_2884877
Anti-Rab29 (phospho T71), Rabbit Monoclonal	Abcam	Cat# ab241062; RRID: AB_2884878
Anti-Rab10, Rabbit Monoclonal	Abcam	Cat# ab237703; RRID: AB_2884879
Anti-Rab10 (phospho T73), Rabbit Monoclonal	Abcam	Cat# ab230261; RRID: AB_2811274
Anti-Rab10 (phospho T73), Rabbit Monoclonal (for IF staining)	Abcam	Cat# ab241060; RRID: AB_2884876
Anti-Rab8A, Rabbit Monoclonal	Cell Signaling	Cat# 6975; RRID: AB_10827742
Anti-Rab8A (phospho T72), Rabbit Monoclonal	Abcam	Cat# ab230260; RRID: AB_2814988
Anti-Rab12, Rabbit Polyclonal	Proteintech	Cat# 8843-1-AP; RRID: AB_10603469
Anti-Rab12 (phospho S106), Rabbit Monoclonal	Abcam	Cat# ab256487; RRID: AB_2884880
Anti-LC3B, Rabbit Polyclonal	Abcam	Cat# ab168831;RRID: AB_2890073
Anti-GM130, Mouse Monoclonal	BD Biosciences	Cat# 610823; RRID: AB_398142
Anti-JIP3, Mouse Monoclonal	Santa Cruz	Cat# sc-46663; RRID: AB_627840
Anti-JIP4/SPAG9, Rabbit Monoclonal	Cell Signaling	Cat# 5519; RRID: AB_10828724
Anti-JIP4, Mouse Monoclonal	Santa Cruz	Cat# sc-271492; RRID: AB_10659098
Anti-Kinesin Heavy Chain, Mouse Monoclonal	EMD millipore	Cat# MAB1614; RRID: AB_94284
Anti-p150 [Glued], Mouse Monoclonal	BD Biosciences	Cat# 610474; RRID: AB_397846
Anti-Arf6, Rabbit Polyclonal	Abcam	Cat# ab77581; RRID: AB_2058475
Anti-Rabbit IgG-IRDye 800CW, Donkey Polyclonal	Li-COR Biosciences	Cat# 926-32213; RRID: AB_621848
Anti-Rabbit IgG-IRDye 680RD, Donkey Polyclonal	Li-COR Biosciences	Cat# 926-68073; RRID: AB_10954442
Anti-Mouse IgG-IRDye 800CW, Donkey Polyclonal	Li-COR Biosciences	Cat# 926-32212; RRID: AB_621847
Anti-Mouse IgG Light Chain-AlexaFluor680, Goat Polyclonal	Jackson Immuno Research Labs	Cat# 115-625-174; RRID: AB_2338937
Bacterial and virus strains		
BacMam mEGFP-LC3	Thermo Fisher	Cat# P36235
NEB Turbo Competent *E. coli*	New England Biolabs	Cat# C2984
Chemicals, peptides, and recombinant proteins		
MLi-2	Tocris	Cat# 5756
DMSO	Sigma-Aldrich	Cat# D2650
Janelia Fluor 646 HaloTag	Promega	Cat# GA1120
PLL (mol wt 70,000 – 150,000)	Sigma-Aldrich	Cat# P1274
HBSS (10x)	Thermo Fisher	Cat# 14185-052
1M HEPES	Thermo Fisher	Cat# 15630-080
2.5% Trypsin	Thermo Fisher	Cat# 15090-046
Minimum essential medium (MEM)	Thermo Fisher	Cat# 11095-072
Horse serum (heat inactivated)	Thermo Fisher	Cat# 16050-122

(*Continued on next page*)

Continued

REAGENT or RESOURCE	SOURCE	IDENTIFIER
Sodium pyruvate	Corning	Cat# 36017004
D-Glucose solution 45%	Sigma-Aldrich	Cat# G8769
GlutaMAX	Thermo Fisher	Cat# 35050061
B27 Supplement	Thermo Fisher	Cat# 17504-044
Neurobasal Medium	Thermo Fisher	Cat# 21103-049
Penicillin-Streptomycin	Thermo Fisher	Cat# 15140-122
AraC	Sigma-Aldrich	Cat# C6645
Lipofectamine 2000 Transfection Reagent	Thermo Fisher	Cat# 11668019
Matrigel Growth Factor Reduced	Corning	Cat# 354230
Essential 8 Medium	Thermo Fisher	Cat# A1517001
mTeSR Medium	StemCell Technologies, Inc.	Cat# 85850
ReLeSR	StemCell Technologies, Inc.	Cat# 05872
Accutase	StemCell Technologies, Inc.	Cat# 07920
ROCK Inhibitor Y-27632	Selleckchem	Cat# S1049
Tet System Approved FBS	Takara	Cat# 631107
DMEM/F-12, HEPES	Thermo Fisher	Cat# 11330032
N2 Supplement	Thermo Fisher	Cat# 17502048
Non-essential Amino Acids (NEAA)	Thermo Fisher	Cat# 11140050
Doxycycline	Sigma-Aldrich	Cat# D9891
Poly-L-Ornithine	Sigma-Aldrich	Cat# P3655
BrainPhys Neuronal Medium	StemCell Technologies, Inc.	Cat# 05790
Laminin	Corning	Cat# 354232
BDNF	PeproTech	Cat# 450-02
NT-3	PeproTech	Cat# 450-03
Lipofectamine Stem Transfection Reagent	Thermo Fisher	Cat# STEM00003
Guanosine-50-[(ab)-methyleno] triphosphate, sodium salt (GMPCPP)	Jena Bioscience	NU-405
AMP-PNP	Sigma-Aldrich	A2647
Microcystin-LR	Sigma-Aldrich	475815
Halt Protease and Phosphatase Inhibitor Cocktail	Thermo Fisher	78442
Critical commercial assays		
BCA Protein Assay Kit	Thermo Fisher	Cat# 23225
Plasmid Maxi Kit	QIAGEN	Cat# 12163
Experimental models: Cell lines		
Human: NGN2 iPSCs	M. Ward (National Institutes of Health) [76]	N/A
Human: LRRK2-G2019S NGN2 iPSCs (heterozygous)	This paper	N/A
Human: LRRK2-WT NGN2 iPSCs	This paper	N/A
Mouse: LRRK2-G2019S knockin MEFs	This paper	N/A
Experimental models: Organisms/strains		
Mouse: LRRK2-G2019S knockin	Taconic	Model #13940
Mouse: C57BL/6NTac WT	Taconic	Model #B6
Rat: hippocampal neuron cultures from embryonic day 18 rat brains (Sprague Dawley)	University of Pennsylvania Neuron Culture Service Center	N/A
Oligonucleotides		
gRNA for LRRK2-G2019S knockin: TGCTCAGTACTGCTGTAGAATGG	This paper	N/A

(*Continued on next page*)

Continued

REAGENT or RESOURCE	SOURCE	IDENTIFIER
LRRK2-G2019S ssDNA HDR template: TTTTCACACTGTATCCCAATGCTGCCA TCATTGCAAAGATTGCTGACTACAGCA TTGCGCAATATTGCTGCCGGATGGGG ATAAAAACATCAGAGGGCACACCAGG TAGGTGATCAGGTCTGTC	This paper	N/A
LRRK2-WT ssDNA HDR template: TTTTCACACTGTATCCCAATGCTGCCA TCATTGCAAAGATTGCTGACTACGGCA TTGCGCAATATTGCTGCCGGATGGGG ATAAAAACATCAGAGGGCACACCAGG TAGGTGATCAGGTCTGTC	This paper	N/A
Recombinant DNA		
Plasmid: EGFP-LRRK2-WT	Modified from FLAG-LRRK2-WT (gift from W. Smith, Johns Hopkins)	N/A
Plasmid: EGFP-LRRK2-G2019S	Modified from FLAG-LRRK2-G2019S (gift from W. Smith, Johns Hopkins)	N/A
Plasmid: EGFP-LRRK2-G2019S-D1994N	Modified from FLAG-LRRK2-G2019S-D1994N (gift from W. Smith, Johns Hopkins)	N/A
Plasmid: mCherry-LC3B	Modified from EGFP-LC3 (gift from T. Yoshimori, Osaka University, Japan)	N/A
Plasmid: PGK EGFP-LC3B	Modified from PGK mCherry-LC3B (gift from Michael Ward, NIH)	N/A
Plasmid: mCherry-EGFP-LC3B	Gift from T. Johansen, University of Tromso, Norway	N/A
Plasmid: EGFP-Rab29	Gift from D. Alessi (D. Alessi (University of Dundee, United Kingdom)	N/A
Plasmid: Halo-Rab29	Modified from EGFP-Rab29	N/A
Plasmid: EGFP-Rab5	Gift from M. Zerial (Max Planck Institute, Dresden)	N/A
Plasmid: LAMP1-RFP	Gift from W. Mothes (Yale)	Addgene #1817
Plasmid: SEP-LAMP1-RFP	Gift from J. Bonifacino (NIH)	N/A
Plasmid: EB3-mCherry	Gift from A. Akhmanova (Utrecht University)	N/A
Plasmid: Halo-JIP4	This paper	Modified from MRC PPU #DU27651
Software and algorithms		
FIJI	NIH, USA	https://imagej.net/Fiji
Kymograph Clear 2.0 (FIJI plugin)	[80]	https://sites.google.com/site/kymographanalysis/
Prism 8	GraphPad	https://www.graphpad.com/scientific-software/prism/
MATLAB R2018b	MathWorks	https://www.mathworks.com/products/matlab.html
KymoSuite (custom MATLAB script)	[79]	https://github.com/jnirschl/kinesin-3_guedes-dias_2018/tree/master/kymoSuite
Volocity	PerkinElmer	https://www.perkinelmer.com
Adobe Illustrator 2021	Adobe	https://www.adobe.com/products/illustrator.html
Other		
35 mm #1.5 glass bottom imaging dishes, 14 mm glass diameter	MatTeK	Cat# P35G-1.5-14-C
35 mm #1.5 glass bottom imaging dishes, 20 mm glass diameter	MatTek	Cat# P35G-1.5-20-C

RESOURCE AVAILABILITY

Lead contact

Further information and requests for resources and reagents should be directed to and will be fulfilled by the Lead Contact, Erika Holzbaur (holzbaur@pennmedicine.upenn.edu).

Materials availability

Plasmids and iPSC lines generated in this study are available upon request to the lead contact.

Data and code availability

The custom MATLAB scripts used in this study to manually track kymographs (KymoSuite) are available at https://github.com/jnirschl/kinesin-3_guedes-dias_2018/tree/master/kymoSuite.

EXPERIMENTAL MODEL AND SUBJECT DETAILS

Primary neuron culture

Mouse cortex was dissected from homozygous LRRK2-G2019S or WT embryos of either sex at day 15.5. All experiments were performed following protocols approved by the Institutional Animal Care and Use Committee at the University of Pennsylvania. LRRK2-G2019S knockin mice (model #13940) and B6NTac (model #B6) were obtained from Taconic, Cambridge City, Indiana production site. Cortical neurons were isolated by digestion with 0.25% Trypsin and trituration through a small-bore serological pipette. Rat hippocampal neurons from E18 Sprague Dawley rats were obtained from the Neuron Culture Service Center at the University of Pennsylvania. Neurons were plated in Attachment Media (MEM supplemented with 10% horse serum, 33 mM D-glucose and 1 mM sodium pyruvate) on poly-L-lysine coated 35 mm glass-bottom imaging dishes (P35G-1.5-20-C; MatTek). After 5 h, Attachment Media was replaced with Maintenance Media (Neurobasal [GIBCO] supplemented with 2% B-27 [GIBCO], 33 mM D-glucose [Sigma], 2 mM GlutaMAX [GIBCO], 100 U/mL penicillin and 100 mg/mL streptomycin [Sigma]). AraC (1 μM) was added the day after plating to prevent glia cell proliferation. Every 3-4 days, 40% of the media was replaced with fresh Maintenance Media. Transfections of mouse cortical neurons (DIV 6-7) or rat hippocampal neurons (DIV 6) were performed 16–24 h before imaging with Lipofectamine 2000 Transfection Reagent (ThermoFisher) and 0.4–1.0 μg of total plasmid DNA. For transduction with EGFP-LC3B, mouse cortical neurons (125,000 cells per imaging dish) were incubated with BacMam EGFP-LC3B reagent (ThermoFisher, P36235) 48 h before imaging.

Human iPSC culture and neuronal differentiation

Human i^{3}N iPSCs that harbor a doxycycline-inducible mNGN2 transgene in the AAVS1 safe-harbor locus were a gift from M. Ward (National Institutes of Health, Maryland) and have been described previously.[34,83] Cytogenetic analysis of G-banded metaphase cells demonstrated a normal male karyotype (Cell Line Genetics). Mycoplasma testing was negative. i^{3}N iPSCs were cultured on Growth Factor Reduced Matrigel (Corning) coated plates and fed daily with Essential 8 medium (ThermoFisher). Differentiation into i^{3}Neurons was performed following an established protocol.[36] In brief, i^{3}N iPSCs were split with Accutase (Sigma) and plated on Matrigel-coated dishes in Induction Medium (DMEM/F12 containing 2 μg/mL doxycycline, 1% N2-supplement [GIBCO], 1% NEAA [GIBCO] and 1% GlutaMAX [GIBCO]). After 3 days, pre-differentiated i^{3}Neurons were dissociated with Accutase and cryo-preserved. On day of use, pre-differentiated i^{3}Neurons were thawed and plated on poly-L-ornithine coated live-imaging dishes (MatTek) at a density of 300,000 cells per dish. For each experimental condition, cells from at least two different batches of induction were used. i^{3}Neurons were cultured in BrainPhys Neuronal Medium (StemCell) supplemented with 2% B27 (GIBCO), 10 ng/mL BDNF (PeproTech), 10 ng/mL NT-3 (PeproTech) and 1 μg/mL Laminin (Corning). Every 3-4 days, 40% of the medium was replaced with fresh culture medium. Live-imaging experiments were performed 21 days after thawing pre-differentiated i^{3}Neurons (DIV21). i^{3}Neurons were transfected 72 h before live-imaging with Lipofectamine Stem Transfection Reagent (ThermoFisher) and 1 μg of plasmid DNA.

METHOD DETAILS

Plasmids

Plasmids used include EGFP-LRRK2-WT (subcloned from FLAG-LRRK2-WT, gift from W. Smith, Johns Hopkins University, Maryland), EGFP-LRRK2-G2019S (subcloned from FLAG-LRRK2-G2019S, gift from W. Smith, Johns Hopkins University, Maryland), EGFP-LRRK2-G2019S-D1994N (subcloned from FLAG-LRRK2-G2019S-D1994N, gift from W. Smith, Johns Hopkins University, Maryland), mCherry-LC3B (subcloned from EGFP-LC3, a gift from T. Yoshimori, Osaka University, Japan), PGK mCherry-LC3B (gift from Michael Ward, National Institutes of Health, Maryland), PGK EGFP-LC3B (subcloned from PGK mCherry-LC3B), mCherry-EGFP-LC3B (gift from T. Johansen, University of Tromso, Norway), EGFP-Rab29 (gift from D. Alessi, University of Dundee, United Kingdom), Halo-Rab29 (subcloned from EGFP-Rab29), EGFP-Rab5 (gift from M. Zerial, Max Planck Institute Dresden, Germany), LAMP1-RFP (Addgene #1817), EB3-mCherry (gift from A. Akhmanova, Utrecht University, the Netherlands), Halo-JIP4 (subcloned from pGEXP1-JIP4 #DU27651, acquired from MRC PPU Reagents and services, University of Dundee), SEP-LAMP1-RFP (kindly provided by J. Bonifacino, NIH, Bethesda). Unless stated otherwise plasmids used CMV promoter to initiate transcription.

Generation of LRRK2-G2019S knockin iPSCs

For CRISPR/Cas9 gene editing, i^{3}N iPSCs were cultured on Matrigel coated plates in mTeSR medium (StemCell). Cells were transfected using Lipofectamine Stem Transfection Reagent (TermoFisher) with plasmids encoding Cas9-GFP and gRNA (5′-3′ sequence: TGCTCAGTACTGCTGTAGAATGG), as well as with ssDNA template for homology-directed repair. To generate clones heterozygous for G2019S mutation, iPSCs were transfected with a mix of ssDNA template with and without mutation.[84] After 48 h, iPSCs were sorted through FACS and GFP+ cells were plated on a Matrigel-coated 10 cm dish. Cells were grown for 10 days, then individual colonies were picked and screened for successful gene editing through a restriction site that was introduced as a silent mutation in the ssDNA repair template. Successful editing was confirmed by Sanger sequencing. Karyotype analysis (Cell Line Genetics) demonstrated a normal karyotype for all clones used in this study.

Live-cell imaging

Primary rat hippocampal neurons and mouse cortical neurons were imaged on DIV7-8 in low fluorescence Hibernate E medium (Brain Bits) supplemented with 2% B27 and 2 mM GlutaMAX. i^{3}Neurons were imaged on DIV21 in low fluorescence Hibernate A medium (BrainBits) supplemented with 2% B27, 10 ng/mL BDNF and 10 ng/mL NT-3. Neurons were imaged in an environmental chamber at 37°C on a PerkinElmer UltraView Vox Spinning Disk Confocal system with a Nikon Eclipse Ti inverted microscope. Images were acquired with a Hamamatsu EMCCD C9100-50 camera controlled by Volocity software. Axons were identified based on morphological parameters.[34,85] LC3 vesicles in mouse cortical neurons and i^{3}Neurons, Rab5 vesicles, Rab29 vesicles, and EB3 comets were imaged with a Plan Apochromat 60x 1.40 NA oil immersion objective. LC3 vesicles in rat hippocampal neurons and LAMP1 vesicles were imaged using an Apochromat 100x 1.49 NA oil immersion objective. Time lapse recordings were acquired at a frame rate of 3 frames/sec for 5 min (LAMP1-RFP vesicles), 1.5 frames/sec for 5 min (SEP-LAMP1-RFP vesicles), 1 frame/sec for 5 min (EGFP-LC3 vesicles in mouse cortical and i^{3}Neurons), 1 frame/sec for 3 min (mCherry-LC3 vesicles in rat hippocampal neurons), 0.8 frames/sec for 5 min (EGFP-Rab5/Rab29 + mCherry-LC3 co-trafficking, EGFP-LC3 + Halo-JIP4 co-trafficking, EGFP-LC3 + LAMP1-RFP co-trafficking, mCherry-EGFP-LC3 vesicles), or 0.5 frames/sec for 10 min (EB3-mCherry comets). Representative Halo-JIP4 images shown in Figure 7A were denoised using the "Despeckle" function in ImageJ. Recordings were acquired in the mid-axon (> 300 μm from soma and > 100 μm from distal axon terminal) unless stated otherwise. To aid visualization and accurate quantification of LAMP1-RFP vesicles, the area of interest was photobleached prior to the start of image acquisition using UltraView Photokinesis Device (PerkinElmer). For the Rab29 FRAP assay, Halo-Rab29 signal was photobleached ~10 μm proximal to distal of an axonal EGFP-LC3 vesicle. Halo-Rab29 and EGFP-LC3 signal were recorded at a frame rate of 0.8 frames/sec for 30 s before and 10 min after photobleaching.

Autophagosome isolation assay

Enriched autophagosome fractions were isolated following a protocol modified from Strømhaug et al.[48] Briefly, one mouse brain was collected in a buffered 250mM sucrose solution, homogenized using a tissue grinder, and subsequently subjected to three differential centrifugations through Nycodenz and Percoll discontinuous gradients to isolate vesicles of the appropriate size and density. Following collection, the autophagosome enriched fraction (AP) was divided into three, one third was treated with 10 μg Proteinase K for 45 min at 37°C to degrade non-membrane protected proteins and enrich for internal autophagosome cargo (AP+PK), one third was membrane permeabilized by the addition of 0.2% Triton X-100 prior to the same Proteinase K treatment as a negative control (AP+Tx+PK), and the other third was left untreated for identification of all internal and externally-associated proteins on autophagosomes. For subsequent protein analysis, the input and the autophagosome enriched fractions were lysed in a buffer with a final concentration of 0.5% NP-40 with 1x protease and phosphatase inhibitors, PMSF and Pepstatin A. Protein concentration was measured by Bradford assay and equal amounts of protein in denaturing buffer were run on SDS-PAGE gels for further analysis by Western blot.

Microtubule pelleting assay

WT or G2019S KI MEFs were lysed with BRB80 (80 mM PIPES, 1 mM EGTA, and 1 mM MgCl2) lysis buffer containing 0.5% Triton X-100, 2x Halt Protease and Phosphatase Inhibitor Cocktail (Thermo Fisher), and 2 μg/mL microcystin-LR (Sigma). For LRRK2 kinase inhibition, G2019S KI MEFs were treated with DMSO or 200 nM MLi-2 overnight before lysis. Lysates were incubated with 5 μM GMPCPP-stabilized microtubules at 37°C for 20 min, then centrifuged at 38,400 x g for 20 min at 25°C. Subsequently, pellet and supernatant were separated, and analyzed per SDS-PAGE as described below.

Immunoblotting

Neurons were washed twice with ice cold PBS and lysed with RIPA buffer (50 mM Tris-HCl, 150 mM NaCl, 0.1% Triton X-100, 0.5% deoxycholate, 0.1% SDS, 2x Halt Protease and Phosphatase inhibitor, 2 μg/mL microcystin-LR). Samples were centrifuged for 10 min at 17,000 g, and protein concentration of the supernatant was determinied by BCA assay. Proteins were resolved on 8% (LRRK2) - 15% (Rab proteins) acrylamide gels. Proteins were transferred to Immobilon-FL PVDF membranes (Millipore) using a wet blot transfer system. Membranes were then stained for total protein using Li-Cor Revert Total Protein Stain. Following imaging of total protein stain, membranes were destained, blocked for 1 hr with TrueBlack WB Blocking Buffer (Biotium), and incubated with primary antibodies diluted in TrueBlack WB Antibody Diluent + 0.2% Tween-20 (Biotium) overnight at 4°C. After three washes with TBS-Tween, membranes were incubated with secondary antibodies diluted in TrueBlack WB Antibody Diluent + 0.2% Tween-20 and

0.01% SDS for 1 hr at RT. Following three more washes with TBS-Tween, membranes were imaged using Odyssey CLx Infrared Imaging System (LI-COR). Western Blots were analyzed with Image Studio Software (Li-Cor).

Immunostaining

Mouse cortical neurons were fixed and permeabilized for 8 min at −20°C using ice-cold methanol. Cells were washed three times with PBS and blocked for 1.5 h with 5% goat serum and 1% BSA in PBS. Neurons were then incubated in primary antibodies diluted in blocking solution overnight at 4°C, washed three times with PBS, and incubated in secondary antibodies diluted in blocking solution for 1 h at RT. After three washes with PBS and nuclear counterstaining with Hoechst (ThermoFisher, H21492), coverslips were mounted in ProLong Glass Antifade mountant (ThermoFisher, P36980). Images were acquired as z stacks at 200 nm step-size using an Apochromat 100x 1.49 NA oil immersion objective on the Perkin Elmer spinning disk confocal setup described above.

QUANTIFICATION AND STATISTICAL ANALYSIS

LC3 and LAMP1 vesicle motility

Kymographs of LC3, Rab29, JIP4, and LAMP1 vesicles were generated with the Multiple Kymograph plugin for FIJI using a line width of 5 pixels. Vesicle tracks were traced manually with a custom MATLAB GUI (KymoSuite). Motile vesicles were scored as anterograde (net displacement > 10 μm in the anterograde direction within time lapse acquistion) or retrograde (net displacement > 10 μm in the retrograde direction). Non-motile vesicles were binned into bidirectional (net displacement < 10 μm, but total displacement > 10 μm) and stationary vesicles (net and total displacement < 10 μm). A pause was defined as a single or consecutive instantaneous velocity value of < 0.083 μm/sec.[86] Bidirectional and stationary vesicles were excluded from the quantification of pause number, pause duration, and fraction of time paused. A reversal was defined as a change of movement direction succeeded by a run > 1 μm in the opposing direction. For quantification of Δ run length, the net run length of each vesicle was subtracted from its total run length. Analysis of LC3 vesicles in rat hippocampal neurons was performed unblinded, all other analyses were performed by a blinded investigator.

EB3 dynamics

Kymographs were generated using the KymographClear 2.0 macro toolset as previously described.[86,87] KymographClear passes a Fourier filter on the original kymograph and allows for automated discrimination between anterograde, retrograde, or static components. The transformation improves signal-to-noise ratio of EB3 comets without affecting quantitative analysis of the data. All kymographs of EB3 comets shown in this paper are forward Fourier-filtered kymographs. Tracks of individual EB3 comets were manually traced using KymoSuite MATLAB GUI and used to quantify run-length, run-time and velocity of each comet. Analysis was performed by a blinded investigator.

Autophagosome acidification (mCherry-EGFP-LC3 tandem construct)

Time lapse series were recorded in the proximal (< 150 μm from the cell soma) and distal axon (region immediately proximal to the axon tip). Kymographs were generated using the Multiple Kymograph plugin for FIJI as described above. Traces of LC3 vesicles were counted first in the EGFP, then in the mCherry kymograph by a blinded investigator.

Late endosome/lysosome acidification (SEP-LAMP1-RFP construct)

Time lapse series were recorded in the mid-axon. Kymographs were generated using the Multiple Kymograph plugin for FIJI. Traces of LAMP1 vesicles were counted first in the SEP, then in the RFP kymograph by a blinded investigator.

Rab29 FRAP assay

Halo-Rab29 fluorescence intensity of axonal autophagosomes was measured within a circular area of interest with 0.65 μm diameter. The localization of autophagosomes before and after Halo-Rab29 photobleaching was determined by their (not photobleached) EGFP-LC3 signal. Fluorescence intensity of Halo-Rab29 was quantified in every 5th frame (= every 6.25 s) of the acquired time lapse recording.

Statistical analysis

All statistical analyses were performed with GraphPad Prism 9. Data were tested for normality using Shapiro-Wilk test. Non-normally distributed data were analyzed using nonparametric tests. Figure legends contain the statistical test used and specific p values for each quantification. For statistical analysis of the multiple parameters used to quantify trafficking and pausing, Bonferroni correction was used to adjust significance levels for multiple testing. Figure legends indicate where p values < 0.05 were not considered statistically significant due to Bonferroni correction. For all quantifications at least three independent experiments were analyzed. All figures were prepared with Adobe Illustrator 2021.